

Conceptual Study of an Internal Flowpath of a Vertically-Cruising Ramjet

a project presented to
The Faculty of the Department of Aerospace Engineering
San José State University

in partial fulfillment of the requirements for the degree
Master of Science in Aerospace Engineering

by

Ryan Y. Teon

December 2021

approved by

Dr. Periklis Papadopoulos
Faculty Advisor

and

Dr. Derek Lang
Faculty Co-Advisor



SAN JOSÉ STATE
UNIVERSITY

© 2021
Ryan Y. Teon
ALL RIGHTS RESERVED

Abstract

Conceptual Study of an Internal Flowpath of a Vertically-Cruising Ramjet

Ryan Y. Teon

Applications of ramjets have increased in recent years which has renewed interests in ramjet propulsion. By increasing our understanding of internal ramjet flow, ramjets can be implemented more easily for both civil and military applications. As such, the purpose of this project is to conduct a conceptual study for the internal flowpath of a vertically-cruising ramjet. One of the main objectives is to verify an analytically derived ramjet design using computational fluid dynamics (CFD). From our analytically derived ramjet design, multiple meshes were developed for CFD studies to investigate viable meshes and meshing methodologies for our study. CFD simulations were then conducted for the purpose of verifying our analytically derived ramjet and to investigate proper simulation methodologies to form a foundation for future studies involving internal combustible flow for ramjet propulsion systems.

Acknowledgements

I would like to thank Dr. Periklis Papadopoulos, Dr. Derek Lang, and Dr. Fabrizio Vergine for their support and guidance for my graduate studies and for developing my foundation for compressible flow aerodynamics, propulsion, and computational fluid dynamics. Their knowledge and guidance have proved invaluable throughout the course of this project. I would also like to thank my parents Raymond Teon and Sophia Yu for supporting me throughout my academic studies.

Table of Contents

Abstract	i
Acknowledgements	i
Nomenclature	iii
List of Tables	iv
List of Figures	v
1. Introduction	1
1.1 Motivation	1
1.2 Literature Review	2
1.2.1 Ramjet Propulsion	2
1.2.2 ANSYS Fluent for Combustion	2
1.2.3 Fuel Injection	3
1.2.4 Enhancing Turbulent Mixing	4
1.2.5 Findings on Analysis Methodologies	5
1.2.6 Findings on Flow Solvers	6
1.3 Proposal	8
1.4 Methodology.....	9
2. Ramjet Modeling	10
2.1 Preliminary Analytical Findings.....	10
2.2 Initial Internal Flow Simulation	12
2.2.1 Previous Meshes	13
2.2.1.1 Generic Nozzle	13
2.2.1.2 Three Fuel Injectors Mesh.....	14
2.2.1.3 Contoured Nozzle Mesh	16
2.2.1.4 Structured Axisymmetric Mesh	18
2.2.2 Current Mesh – Unstructured Axisymmetric Mesh	19
3. Boundary Conditions and Setup	22
3.1 Boundary Conditions for the Density-Based Solver	22
3.1.1 Boundary Conditions for the Three Fuel Injectors Layout	26
3.2 Boundary Conditions for the Pressure-Based Solver	27
4. Results and Discussion	30
4.1 Preliminary Results	30
4.1.1 Generic Nozzle.....	30

4.1.2 Three Fuel Injectors	33
4.1.3 Contoured Nozzle	35
4.1.4 Structured Axisymmetric Mesh	38
4.2 Current Mesh – Unstructured Axisymmetric Mesh	43
4.2.1 Unstructured Axisymmetric Mesh	43
4.2.2 Unstructured Axisymmetric Mesh with a smaller time step	48
5. Conclusions and Recommendations	54
References	55
Appendix: Coordinate Points for Mach 1.806 Nozzle	57

Nomenclature

Symbol	Definition	Units
M_i	Mach number	
u_i	velocity	m/s
$p_{0,i}$	total pressure	kPa or Pa
p_i	static pressure	kPa or Pa
$T_{0,i}$	total temperature	K
T_i	static temperature	K
m_i	mass	kg
\dot{m}_i	mass flow rate	kg/s
L	length	m or mm
A_i	area	mm^2 or m^2
A^*	choked throat area	mm^2 or m^2
$A_{t,i}$	throat area	mm^2 or m^2
A_c	combustor cross sectional area	mm^2 or m^2
z_i	altitude	km or m
c_D	drag coefficient	
C_p	specific heat	
Y_i	mass fraction	
Greek Symbols		
Φ	equivalence ratio	
γ_i	specific heat ratio	

List of Tables

Table 2.1: Initial parameters and conditions	10
Table 2.2: Freestream conditions when $z = 8,350$ m	12
Table 2.3: Exhaust conditions at end of ramjet when $z = 8,350$ m	12
Table 2.4: Mesh quality metrics for generic mesh	14
Table 2.5: Mesh quality metrics for three-injector mesh	16
Table 2.6: Mesh quality metrics for contoured nozzle mesh	18
Table 2.7: Revised geometry for contoured nozzle mesh	18
Table 2.8: Mesh quality metrics for the structured axisymmetric mesh	19
Table 3.1: Station 3 air inlet conditions	21
Table 3.2: Station 4 conditions	23
Table 3.3: Injector throat dimensions	23
Table 3.4: Hydrogen inlet conditions	24
Table 3.5: Property settings for air inlet	25
Table 3.6: Property settings for hydrogen-air mixture	26
Table 3.7: Property settings for individual elements at inlet	26
Table 3.8: Spatial discretization settings for density-based solver	26
Table 3.9: Individual injector dimensions in three-injector layout	26
Table 3.10: Individual injector conditions in three-injector layout	27
Table 3.11: Revised injector area	28
Table 3.12: Mass flow rates used for air and fuel mass flow inlets	28
Table 3.13: Mole fractions	29
Table 3.14: Spatial discretization settings for pressure-based solver	29
Table 3.15: Mass flow rates used for air and fuel mass flow inlets	29
Table 4.1: Comparison of outlet conditions for the generic nozzle	33
Table 4.2: Comparison of outlet conditions for the contoured nozzle	38
Table 4.3: Comparison of outlet conditions for the structured axisymmetric model	39
Table 4.4: Comparison of outlet conditions for the unstructured axisymmetric model	44
Table 4.5: Comparison of outlet conditions for the unstructured axisymmetric model	49

List of Figures

Figure 1.1: Pressure distribution obtained from Clark’s validation study	3
Figure 1.2: Fuel injection methods	4
Figure 1.3: Flow field of a cavity.....	5
Figure 1.4: Scramjet geometries with flame holders	5
(a) original geometry by German Aerospace Center (DLR)	
(b) spherical cavity	
(c) step cavity	
Figure 1.5: Overview of pressure-based solution algorithms	7
Figure 1.6: Overview of density-based solution algorithm.....	8
Figure 1.7: Ramjet layout.....	9
Figure 2.1: Inlet unstarting at approximately 17 km of altitude	11
Figure 2.2: $\Phi=1$ until 19 km of altitude	11
Figure 2.3: Velocity, mach number, thrust, and mass flow rate with altitude	12
Figure 2.4: Generic nozzle mesh.....	13
Figure 2.5: Closeup of mesh at fuel injector	14
Figure 2.6: Mesh with three fuel injectors	15
Figure 2.7: Three fuel injectors.....	15
Figure 2.8: Closeup of individual fuel injector	16
Figure 2.9: Mesh with contoured nozzle.....	17
Figure 2.10: Fuel injector of contoured nozzle	17
Figure 2.11: Structured axisymmetric mesh	18
Figure 2.12: Meshing area around the nozzle of the structured axisymmetric mesh.....	19
Figure 2.13: Unstructured axisymmetric Mesh.....	20
Figure 2.14: Meshing area around the nozzle of the unstructured axisymmetric mesh.....	20
Figure 2.15: Meshing area around the inlet of the structured axisymmetric mesh.....	21
Figure 3.1: Cross sectional area of combustion chamber	22
Figure 3.2: Species transport settings	25
Figure 3.3: Injector geometry.....	28
Figure 4.1: Mach contours for the generic nozzle	30
Figure 4.2: Mach contours near fuel injector for the generic nozzle	30
Figure 4.3: Static pressure contours for the generic nozzle	31
Figure 4.4: Static temperature contours for the generic nozzle	31
Figure 4.5: Static temperature contours near fuel injector for the generic nozzle	32

Figure 4.6: Residuals for the generic nozzle.....	32
Figure 4.7: Mach contours for three-injector layout with original injector area.....	34
Figure 4.8: Static temperature contours for three-injector layout with original injector area.....	34
Figure 4.9: Closeup of static temperature contours for three-injector layout with original injector area.....	35
Figure 4.10: Mach contours for the contoured divergent nozzle	36
Figure 4.11: Static temperature contours for the contoured divergent nozzle	36
Figure 4.12: Static pressure contours for the contoured divergent nozzle.....	37
Figure 4.13: Residuals for the contoured divergent nozzle	37
Figure 4.14: Mach contours for the structured axisymmetric mesh	38
Figure 4.15: Static temperature contours for the structured axisymmetric mesh	38
Figure 4.16: Static pressure contours for the structured axisymmetric mesh.....	39
Figure 4.17: Drag force near walls for the structured axisymmetric mesh.....	40
Figure 4.18: Area-weighted average of mach number at the outlet for the structured axisymmetric mesh	40
Figure 4.19: Area-weighted average of static temperature at the outlet for the structured axisymmetric mesh	41
Figure 4.20: Area-weighted average of hydrogen at the outlet for the structured axisymmetric mesh	41
Figure 4.21: Area-weighted average of oxygen at the outlet for the structured axisymmetric mesh	42
Figure 4.22: Residuals for the structured axisymmetric mesh.....	42
Figure 4.23: Mach contours for the unstructured mesh	43
Figure 4.24: Static temperature contours for the unstructured mesh	43
Figure 4.25: Static pressure contours for the unstructured mesh.....	44
Figure 4.26: Drag force near walls for the unstructured axisymmetric mesh.....	45
Figure 4.27: Area-weighted average of outlet mach for the unstructured axisymmetric mesh	45
Figure 4.28: Area-weighted average of static temperature at the outlet for the unstructured axisymmetric mesh	46
Figure 4.29: Area-weighted average of hydrogen at the outlet for the unstructured axisymmetric mesh.....	46
Figure 4.30: Area-weighted average of oxygen at the outlet for the unstructured axisymmetric mesh	47
Figure 4.31: Residuals for the unstructured axisymmetric mesh.....	47
Figure 4.32: Mach contours for the unstructured mesh with a reduced time step	48
Figure 4.33: Static pressure contours for the unstructured mesh with a reduced time step.....	48
Figure 4.34: Static temperature contours for the unstructured mesh with a reduced time step	49
Figure 4.35: Drag force near walls for the unstructured mesh with a reduced time step.....	50
Figure 4.36: Area-weighted mach number at the outlet for the unstructured mesh with a reduced time step	50

Figure 4.37: Area-weighted average of static temperature at the outlet for the unstructured mesh with a reduced time step	51
Figure 4.38: Area-weighted average of oxygen at the outlet for the unstructured mesh with a reduced time step	51
Figure 4.39: Area-weighted average of hydrogen at the outlet for the unstructured mesh with a reduced time step	52
Figure 4.40: Area-weighted average of static pressure at the outlet for the unstructured mesh with a reduced time step	52
Figure 4.41: Residuals for the unstructured mesh with a reduced time step	53

1. Introduction

1.1 Motivation

The motivation for conducting a conceptual study of a ramjet is to aid in the design of a ramjet for use on a rocket in vertical high-speed flight during the rocket's airbreathing stage. While analytical simulations can be achieved, such simulations will need to be verified with computational fluid dynamics (CFD) analysis. This will be to verify the overall design of the ramjet by validating the combustion of the air-fuel mixture along with confirming sufficient compression of the incoming air to aid in combustion to generate adequate thrust. Another motivation is to also increase our understanding of ramjets to aid with propulsion analysis and design.

If the internal flowpath of the ramjet is not validated properly, then it could lead to the ramjet failing to function properly. Such issues that could occur could be the inability to generate sufficient thrust which may be caused by issues such as the inlet not sufficiently compressing air or because the combustion chamber is too short to allow for the air and fuel to react and fully combust. Because of this, analytical simulations alone are usually not sufficient to validate the design of a ramjet.

To verify ramjet designs without resorting to expensive measures such as wind tunnel testing or flight testing, ANSYS Fluent will be used to investigate simulation methodologies. While there were initially doubts on whether ANSYS Fluent could be used for such an application, further research has verified the feasibility of ANSYS Fluent for investigating combustion interactions.

Ramjets have numerous practical uses such as on the MBDA Meteor air-to-air missile that is currently used on the Eurofighter Typhoon, Dassault Rafale, and Saab JAS-39 Gripen. Conventional rocket propelled missiles such as the American AIM-120 AMRAAM or the Russian R-77 will gradually lose speed as the missile consumes fuel resulting in a missile that can be evaded by a skilled pilot with adequate equipment. The Meteor on the other hand can regulate thrust delivery with its ramjet to save fuel to ensure that the missile will reach its target at significantly higher speeds to make evasion more difficult [2]. As a result, ramjets are not uncommon for usage on missiles.

As such, the applications of ramjet propulsion also increase the interests behind conceptual studies for ramjets. By increasing our understanding of internal ramjet flow, ramjets can be implemented more easily for both civil and military applications. Increasing our understanding of ramjet propulsion will also act as an appropriate segue into supersonic combustion ramjet (scramjet) design.

1.2 Literature Review

1.2.1 Ramjet Propulsion

A ramjet is a type of airbreathing engine that functions by compressing air at the inlet for ignition with the fuel (gaseous hydrogen in our case). The nozzle at the end of the ramjet will then accelerate the exhaust flow to generate thrust. Because a ramjet relies on incoming air to be compressed by the inlet section, a ramjet cannot produce thrust when it is stationary. As a result, ramjets require secondary methods of propulsion to accelerate the ramjet to appropriate speeds for thrust generation [1]. Rocket propulsion is a common method for accelerating ramjets such as for our case.

1.2.2 ANSYS Fluent for Combustion

One of the questions that was originally asked was whether ANSYS Fluent can simulate reactive flows for our scenario. Thankfully, it appears that ANSYS Fluent is viable for our simulation case. Researchers at the Indian Institute of Technology Madras (IIT Madras) were able to utilize ANSYS Fluent to simulate a scramjet for use on the Hypersonic Technology Demonstrator Vehicle (HSTDV) [3].

The IIT Madras researchers were able to utilize ANSYS Fluent for supersonic combustion which is more intensive than our subsonic combustion ramjet. They were also able to simulate multiphase flow with liquid fuel for their scramjet with a requirement that the fuel is to be mixed, ignited, and burned within 1 millisecond [3]. While our ramjet does not require a multiphase flow simulation because the fuel is gaseous, it does show that multiphase liquid fuel combustion is possible to simulate in ANSYS Fluent if later revisions require liquid fuel injection.

For the simulation of our ramjet the ideal turbulence models for usage will need to be determined since the addition of combustion can affect the viability of a turbulence model. A study on scramjet combustion by Clark compiled a validation study using seven different simulations with seven different turbulence models to validate the experimental and numerical results from an earlier supersonic combustion study. From these findings, all the tested turbulence models follow the same trends as expected from the earlier study [4, 5].

It appears that the turbulence model that produced the least amount of error from the original numerical and experimental values is the Reynolds Stress Model (RSM) using the low-Reynolds stress omega model [4]. This appears to be due to the RSM assuming anisotropy in the Reynolds stresses which affects the flow field and can be valid for flows with high amounts of swirl [6].

Other turbulence models that could also be used are the Standard and Shear Stress Transport (SST) k-omega models. While Figure 1.1 shows a higher amount of error for both standard and SST k-omega models, it is still ideal for wall-bounded flows with the SST variant being particularly viable for the adverse pressure gradients expected within turbulent flows [6]. For the ramjet simulation itself, multiple simulations may be evaluated using different turbulence models to determine which turbulence model would best fit our case.

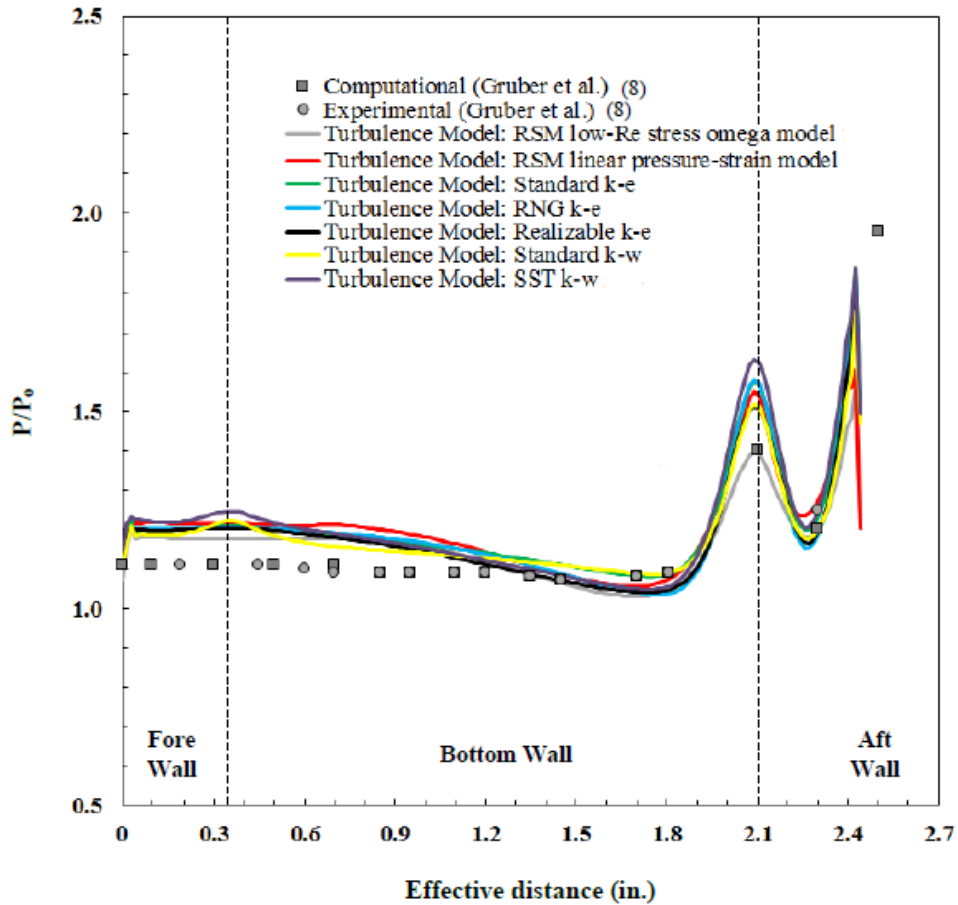


Figure 1.1: Pressure distribution obtained from Clark's validation study [4]

These findings on the effectiveness of ANSYS Fluent for more intensive cases than our ramjet simulation lends credence to the viability of ANSYS Fluent for combustion simulation.

1.2.3 Fuel Injection

While the fuel injection process for our ramjet should not require complicated injection methods due to the subsonic nature of our combustion processes, it is still useful to investigate fuel injection techniques to also determine fuel injector methods for ideal combustion.

Possible methods include a flush-wall type injector where fuel is delivered via ports that are flush with the combustion chamber's walls. However, while flush-wall injectors are less complex than other injection methods, the caveat is that the injected fuel may not sufficiently mix with the incoming air due to the increased distance between the injector and the core of the flow where turbulent mixing would occur [7].

One possible method is ramp injection which delivers fuel by placing the injectors along a ramp for the incoming airflow while also initiating further turbulence to aid with mixing [7]. However, the complexity added by implementing a ramp in a combustion chamber such as ours negates the benefits.

Another method is strut injection where a strut would protrude into the core of the flow to inject fuel. A caveat for strut injection is increased wave drag, however such a concern would only be valid in the case of supersonic combustion which is out of the scope of this project [7, 8]. Despite the increased complexity, strut injection could be viable if it is discovered that the distance between the fuel injector and the core flow of the combustion chamber needs to be reduced. In such a situation, strut-based injection could be implemented with further ease than ramp injection while also improving turbulent mixing compared to flush-wall injection.

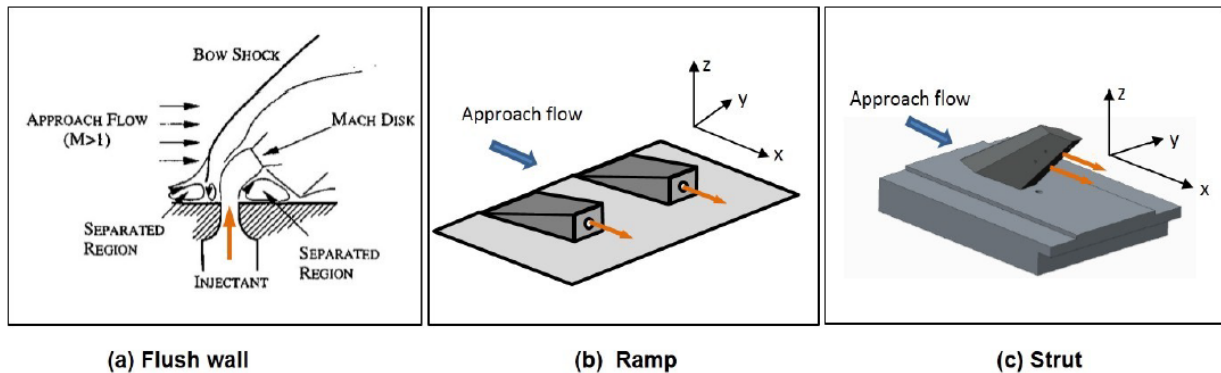


Figure 1.2: Fuel injection methods [7]

1.2.4 Enhancing Turbulent Mixing

Due to the need for continuous combustion in most airbreathing engines it is imperative to maintain and enhance turbulent mixing between the oxidizer and the fuel. Such devices that aid with mixing include flame holders which are commonly used on jet engines to maintain continuous combustion by maintaining turbulent mixing. Certain injection methods can also enhance turbulent mixing [7, 14].

However, flameholders and specialized fuel injectors are not the only features that can enhance mixing. Wall-mounted cavities can greatly enhance turbulent mixing by generating eddies that

increase turbulence in the combustion chamber itself to increase mixing efficiency [4, 10, 14]. While wall mounted cavities may not be needed in our case, it could allow for the combustion chamber to be shortened if needed for space constraints. The caveat to wall-mounted cavities would be the increased complexity to the manufacturing process.

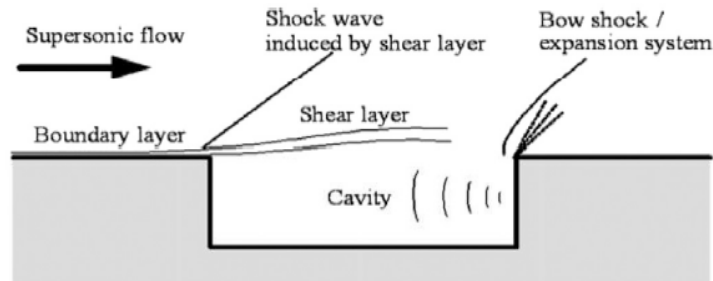


Figure 1.3: Flow field of a cavity [10]

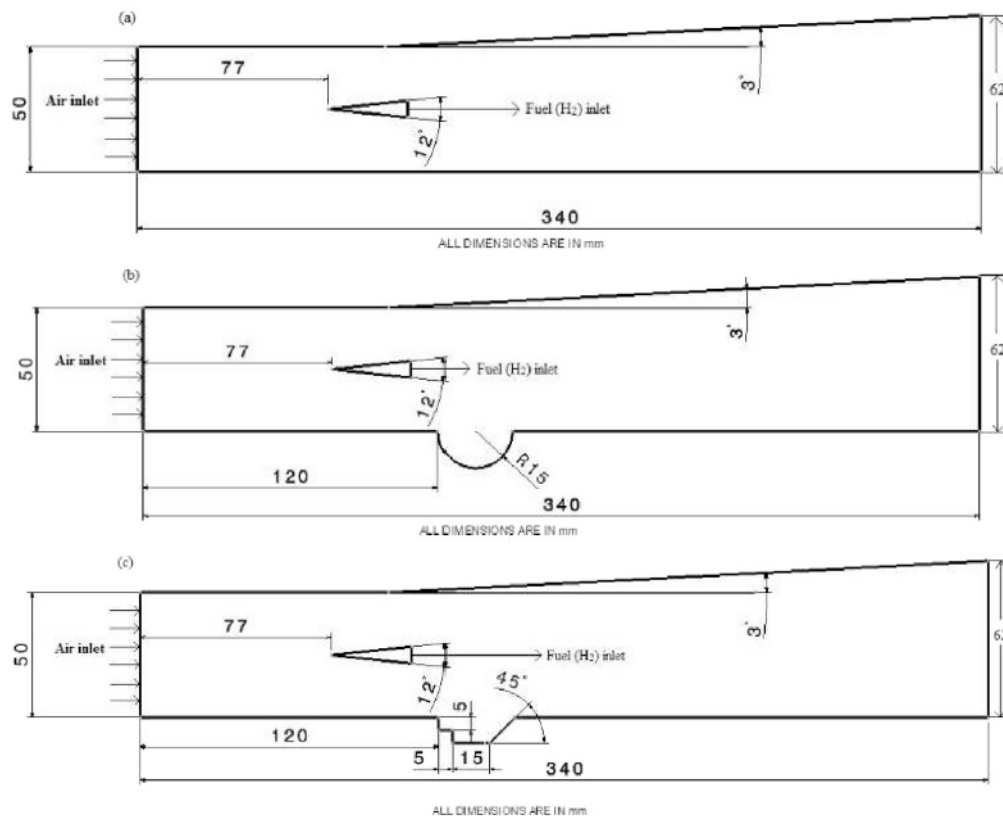


Figure 1.4: Scramjet geometries with flame holders (a) original geometry by German Aerospace Center (DLR) without cavity (b) spherical cavity (c) step cavity [10]

1.2.5 Findings on Analysis Methodologies

To increase our understanding of CFD and computational analysis methods for combustion, we will need to evaluate methodologies that other researchers have used. The expenses behind the computational evaluation of reaction engines are a barrier in propulsion design. This results in

CFD being a common tool for propulsion analysis despite potential issues such as the possibility of the simulation not capturing combustion features properly if invalid simulation models are selected or if the chosen simulation models are improperly used [12].

A Large Eddy Simulation (LES) is a possible method that can be used to analyze turbulent mixing and combustion. The ability for the LES method to capture unsteady phenomena in reactive flows as it occurs in time makes it extremely capable for simulating the internal flowpath of a ramjet. However, LES methods require meshes of extremely high resolution which puts most LES methods out of reach for the computational power available to most people [4, 12, 14]. As such, methodologies that utilize the Reynolds-Averaged Navier-Stokes (RANS) equations (1.1) are more commonly used than LES.

The RANS equations are steady-state, time-averaged equations derived from the Navier-Stokes equations in which the Reynolds Decomposition is applied for simplification into its time-averaged form [6, 9]. Time-averaged methods like RANS are far more commonly used than LES methods for CFD analysis due to the reduced requirements for mesh resolution which result in reduced requirements for computational power [13].

RANS methodologies will be utilized for the internal flowpath analysis of our ramjet. If the appropriate turbulence models are selected for usage along with the appropriate boundary conditions, then the resultant simulations should prove to be accurate.

$$\frac{\partial \rho}{\partial t} + \frac{\partial}{\partial x_i} (\rho u_i) = 0$$

$$\frac{\partial}{\partial t} (\rho u_i) + \frac{\partial}{\partial x_j} (\rho u_j u_i) = -\frac{\partial p}{\partial x_i} + \frac{\partial}{\partial x_j} \left[\mu \left(\frac{\partial u_i}{\partial x_j} + \frac{\partial u_j}{\partial x_i} - \frac{2}{3} \delta_{ij} \frac{\partial u_l}{\partial x_l} \right) \right] + \frac{\partial}{\partial x_j} (-\rho \overline{u'_j u'_i})$$

(1.1)

1.2.6 Findings on Flow Solvers

ANSYS Fluent allows for both pressure-based and density-based flow solvers to be used for simulations with the pressure-based solver being used for low-speed incompressible flows and the density-based solver being used for high-speed compressible flows. While both solvers have been reformulated and altered over the years to increase their capabilities, they are still distinct enough to restrict them to certain flow conditions [20].

The pressure-based solver employs a projection method where the continuity of the velocity field is achieved by solving a pressure equation that is derived from the continuity and momentum equations. The governing equations used are nonlinear and coupled with the solution process involving an iterative process of solving a set of governing equations repeatedly until convergence is reached [20].

A segregated and coupled algorithm are available for the pressure-based solver within ANSYS Fluent with an overview of the pressure-based models being available in Figure 1.5. The segregated algorithm solves the individual governing equations for the solution variables after one another with each governing equation being decoupled or “segregated” from other equations. Afterwards the pressure-corrected continuity equations are then solved [20].

In the coupled algorithm a coupled system of equations comprising of the momentum equations and the pressure-based continuity equation are being solved at the same time unlike in the segregated algorithm. With the remaining equations being solved in a decoupled fashion like the segregated method [20].

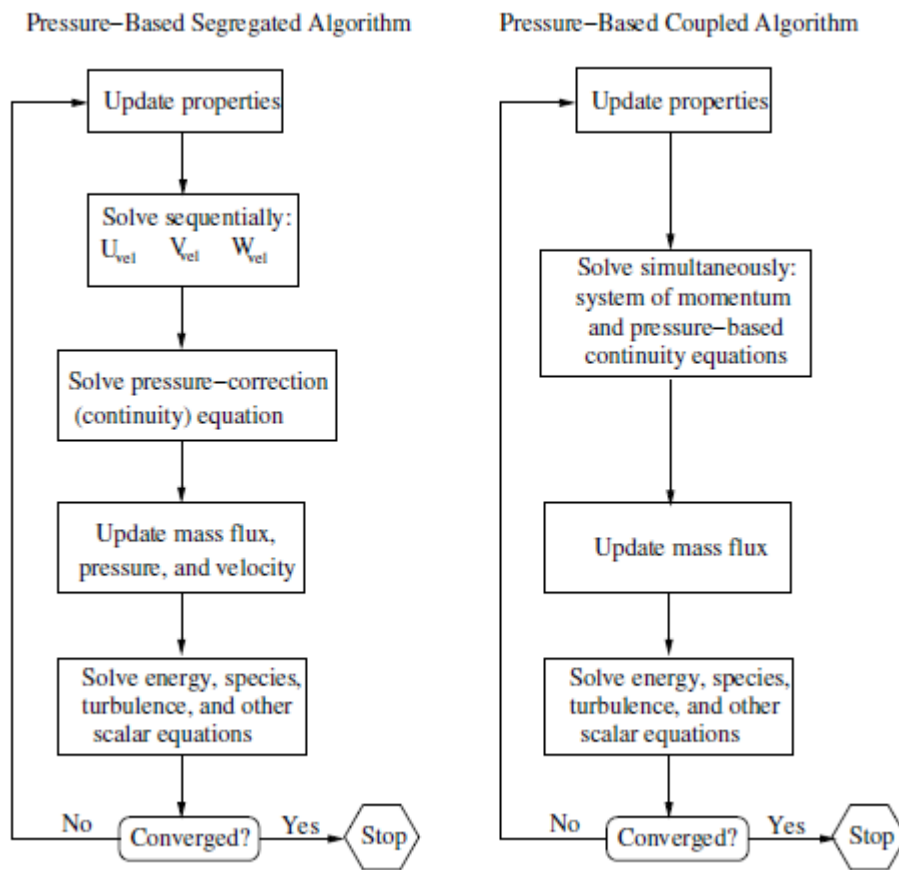


Figure 1.5: Overview of pressure-based solution algorithms [20]

In the density-based solver the governing equations of continuity, momentum, energy, and species transport are coupled together. The fact that the governing equations are formulated from density instead of pressure also makes the density-based solver more suitable for compressible flow simulations. The solution loop is outlined in Figure 1.6 with the solution loop being iteratively solved until a converged solution is obtained [20].

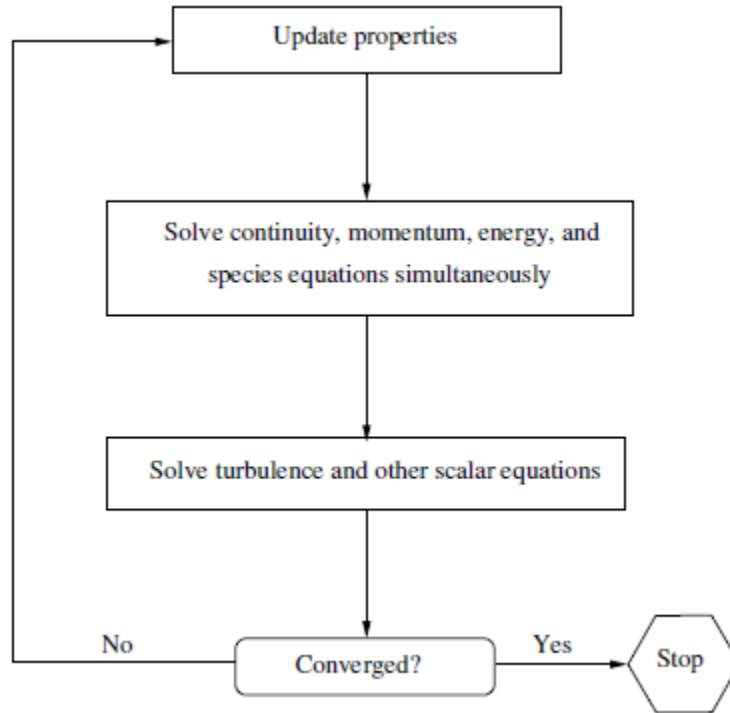


Figure 1.6: Overview of density-based solution algorithm [20]

1.3 Proposal

The primary purpose of this project will be to conduct a conceptual study for the internal flowpath of a vertically-cruising ramjet's internal flow with CFD analysis via ANSYS Fluent. The project is a collaboration with Engineering Space to aid in the design of a rocket that will also utilize ramjet propulsion for its airbreathing stage by verifying the internal flow of the ramjet.

Our focus will be to simulate the combustion chamber and the exhaust nozzle to confirm that the combustion chamber reactions will match our analytical simulation results and to verify the design of the exhaust nozzle. Proper simulation methodologies will be investigated to form a foundation for future internal combustible flow studies to be based off.

1.4 Methodology

The overall methodology will involve utilizing ANSYS Fluent for CFD analysis to simulate the combustion chamber's internal flow to determine whether combustion will occur and if the temperature, pressure, and Mach values will be sufficient for the nozzle of the ramjet to accelerate the exhaust flow to generate adequate thrust. The first steps include investigating which types of meshes, boundary conditions, and CFD models would be appropriate for our analytically derived ramjet.

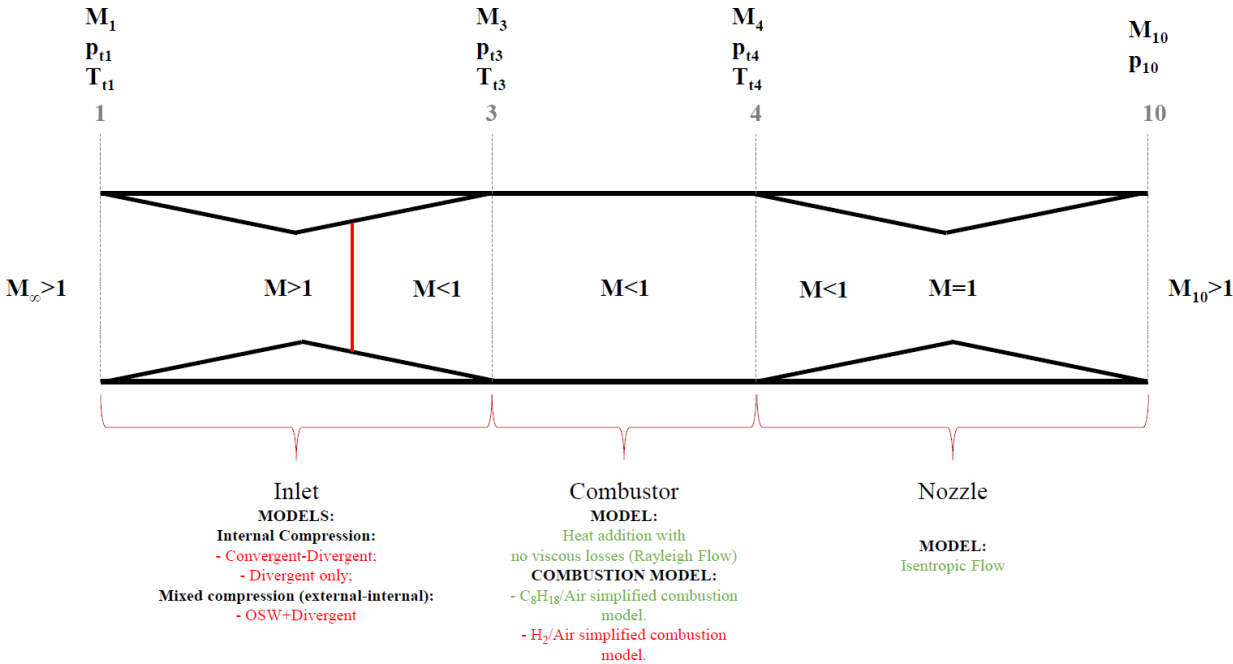


Figure 1.7: Ramjet layout

2. Ramjet Modeling

2.1 Preliminary Analytical Findings

Preliminary analyses were conducted with varied sets of internal geometries and initial conditions. The simulation set that was evaluated for this study is shown in Table 2.1.

Table 2.1: Initial parameters and conditions

Freestream (γ_1)	1.4
Inlet Area (A_1)	64.8 mm \times 125 mm
Diffuser Throat Area ($A_{t,d}$)	49.9 mm \times 125 mm
Combustor Cross Sectional Area (A_c)	125 mm \times 125 mm
Nozzle Exit Area (A_{10})	125 mm \times 125 mm
Nozzle Area Ratio (A_{10}/A_t)	1.5
Fuel	Hydrogen (H_2)
Drag Coefficient (c_D)	0.8
Ramjet Deployment Altitude ($z_{initial}$)	8,350 m
Mach Number at Deployment (M_i)	2.6
Vehicle Mass ($m_{initial}$)	30 kg

It was found that in this configuration, the range of the vehicle was found to be 8.5 km where it would be limited due to the inlet unstarting at an altitude of approximately 17 km despite our equivalence ratio (Φ) being 1 until 19 km [15]. The equivalence ratio is defined as the ratio of the actual fuel to air ratio and the stoichiometric fuel to air ratio where all the oxygen would be consumed [16].

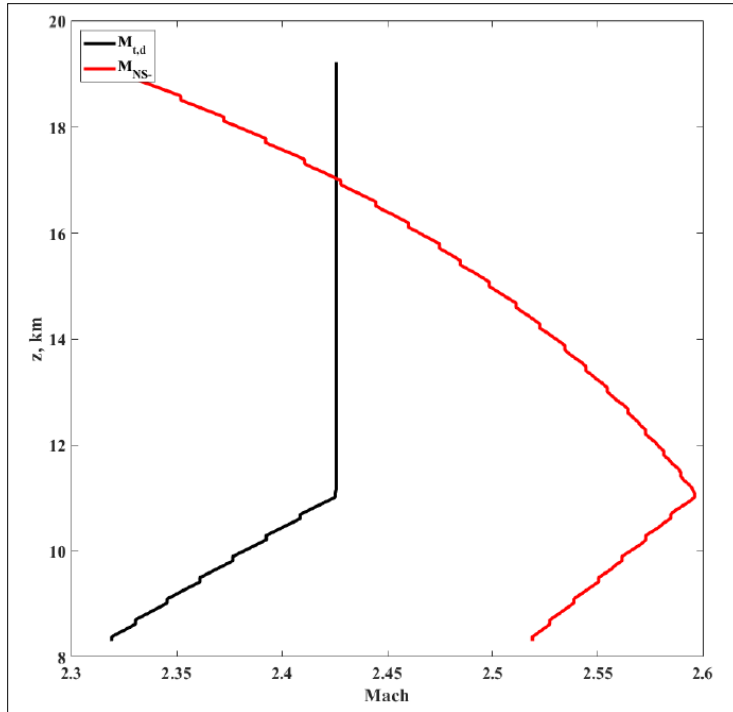


Figure 2.1: Inlet unstating at approximately 17 km of altitude [15]

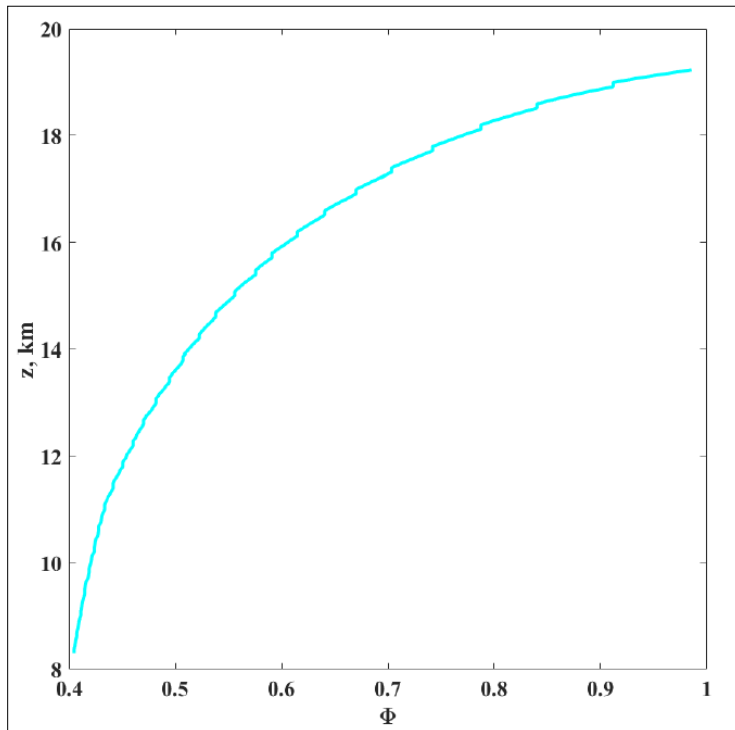


Figure 2.2: $\Phi = 1$ until 19 km of altitude [15]

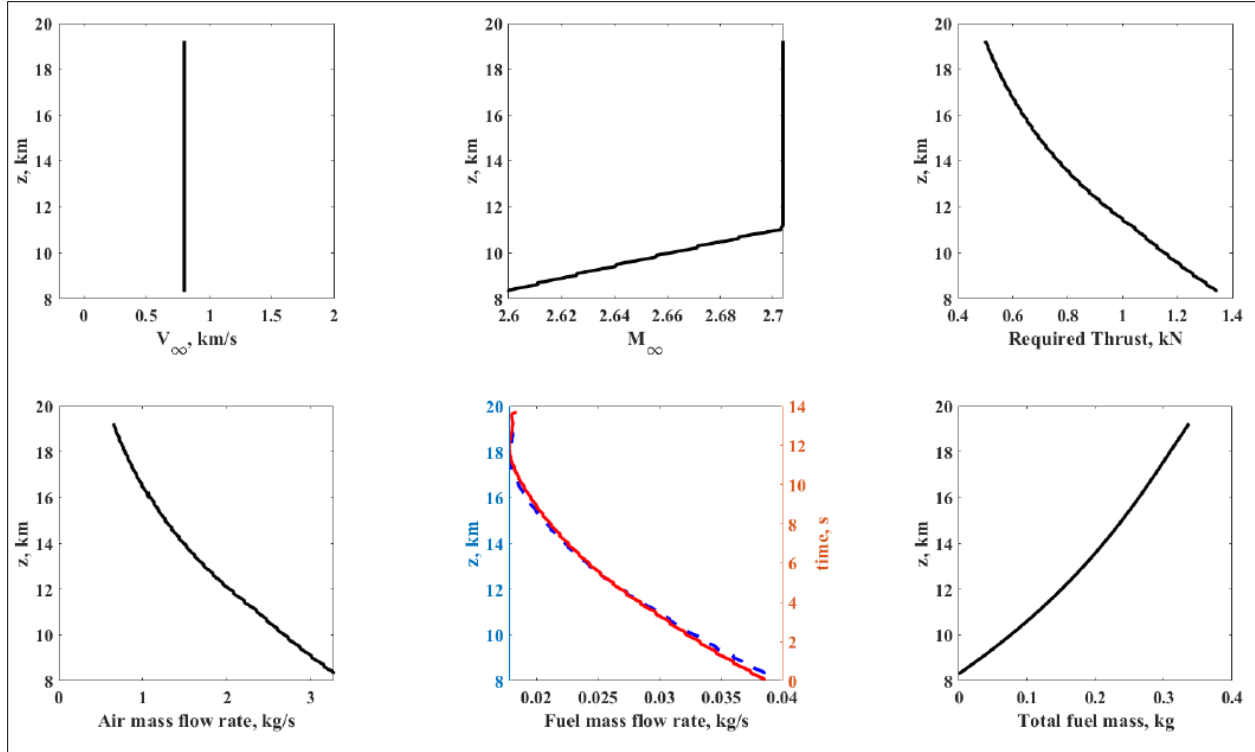


Figure 2.3: Velocity, Mach number, thrust, and mass flow rate with altitude [15]

Analytical simulations were done via Matlab to determine which values are to be expected from the ramjet when it is deployed as shown below [15].

Table 2.2: Freestream conditions when $z = 8,350$ m [15]

M_1	2.6
P_1 (kPa)	34.14
T_1 (K)	234.29
γ_1	1.4
\dot{m}_1 (kg/s)	3.280

Table 2.3: Exhaust conditions at end of ramjet when $z = 8,350$ m [15]

M_{10}	1.806
P_{10} (kPa)	55.47
T_{10} (K)	1106.68
γ_{10}	1.283
\dot{m}_{10} (kg/s)	3.318

2.2 Initial Internal Flow Simulation

To verify our analytical values, a computational simulation was conducted. One of the first steps is to complete a simulation of the combustion chamber to verify if combustion will occur and if

the averaged values at the exit will match the analytically obtained values that were obtained earlier. As seen in Figure 1.7, station 3 will represent the beginning of the combustion chamber while station 4 will represent the end of the combustion chamber before the flow reaches the nozzle of the ramjet.

2.2.1 Previous Meshes

2.2.1.1 Generic Nozzle

Our initial mesh only simulated the combustion chamber and the fuel injector itself. However, due to the erroneous results from the initial mesh, it was determined that a simulation of the convergent-divergent nozzle from station 4 to station 10 as seen in Figure 1.7 was necessary. The results that were generated by this mesh are much more promising than the initial results that only simulated the combustion chamber and fuel injector.

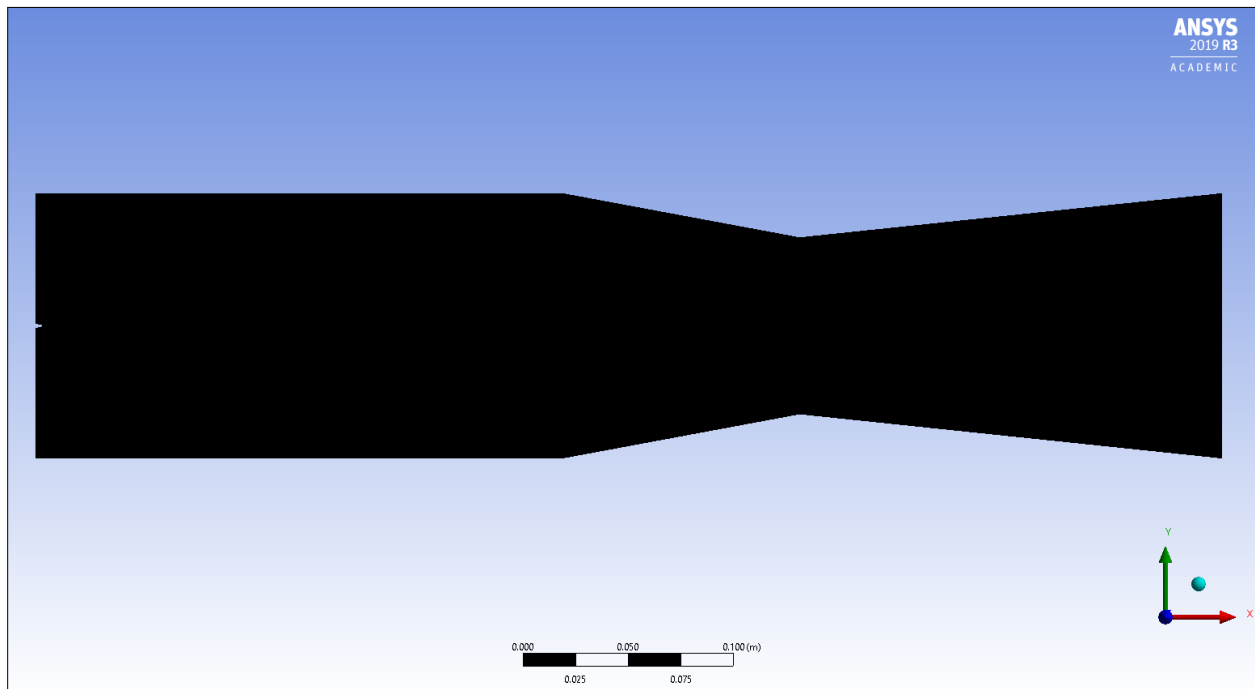


Figure 2.4: Generic nozzle mesh

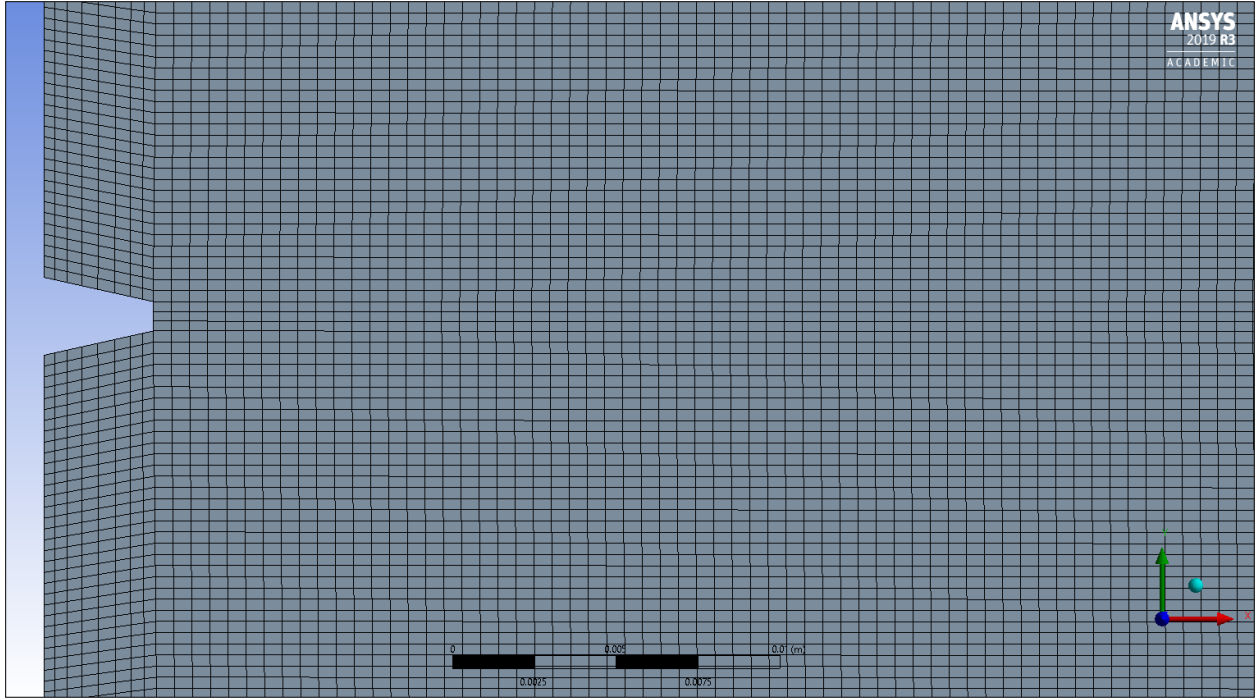


Figure 2.5: Closeup of mesh at fuel injector

The structured mesh utilizes 384,822 elements and models a straight contour converging-diverging nozzle for the exit. We are currently waiting on precise nozzle contours derived from the Method of Characteristics. However, we will work with the straight contour configuration for the time being.

Table 2.4: Mesh quality metrics for generic mesh

Minimum Orthogonal Quality	0.97352
Max Skewness	0.14707
Aspect Ratio	4.3408

For our mesh quality metrics in a structured mesh as seen in Table 2.4, it is ideal to have an orthogonal quality that is as close to one as possible while the max skewness should be as close to zero as possible. The Aspect Ratio should also be as low as possible. The mesh metrics that have been obtained are acceptable for geometry we are simulating.

2.2.1.2 Three Fuel Injectors Mesh

A mesh with three fuel injectors was also implemented to increase turbulent mixing and the combustion chamber was lengthened from 250 mm to 305 mm to allow for adequate reaction time. The throat area for each individual fuel injector was reduced by 1/3 of the original throat area to maintain an overall mass flow rate of 0.038 kg/s.

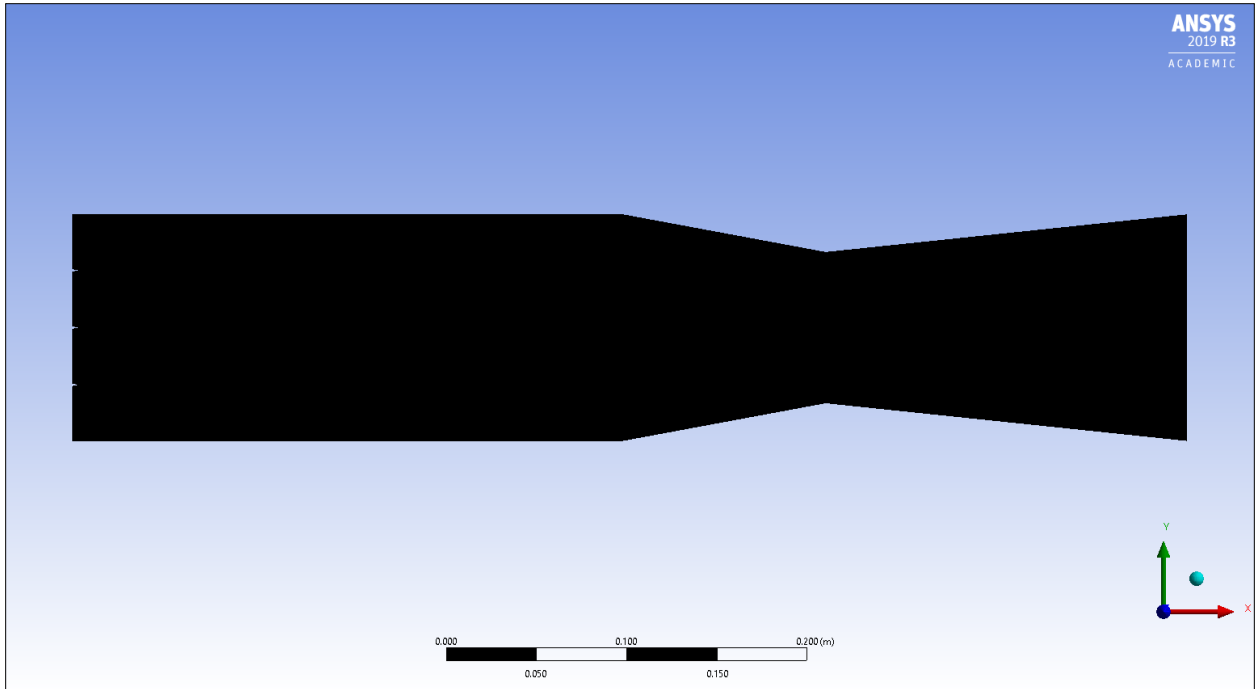


Figure 2.6: Mesh with three fuel injectors

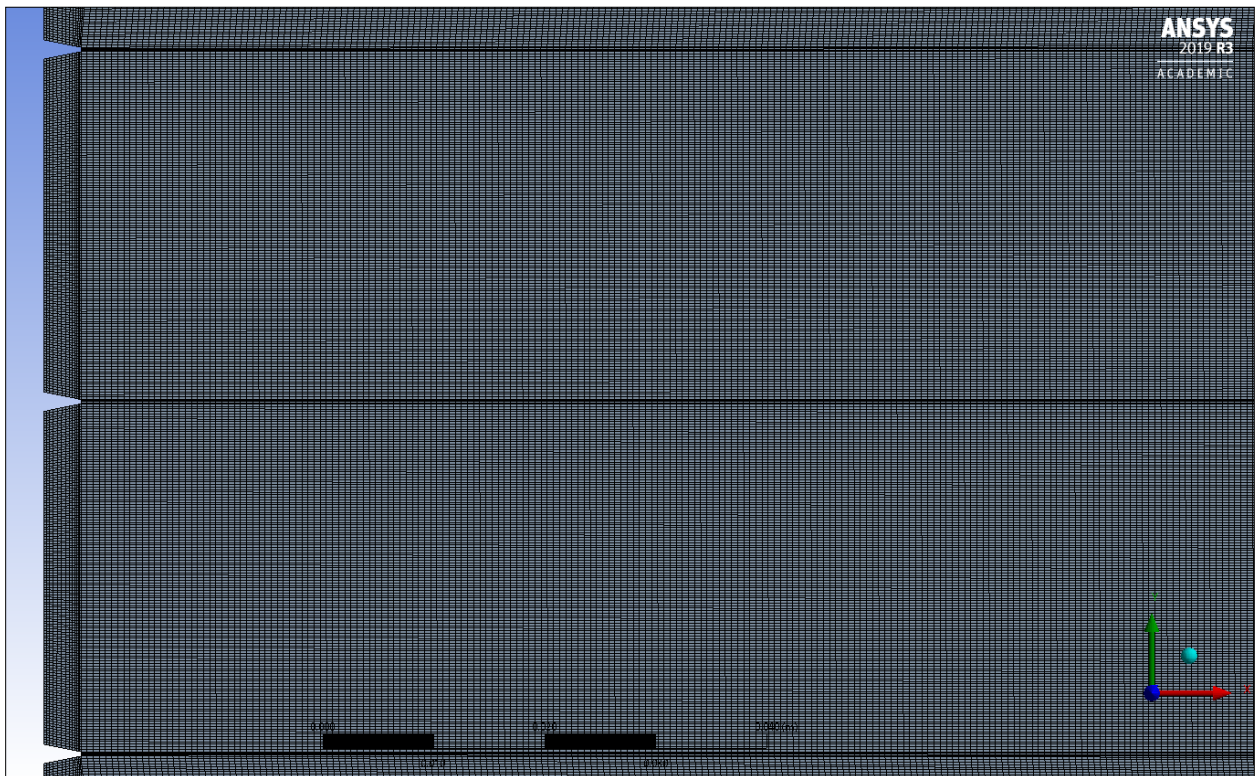


Figure 2.7: Three fuel injectors

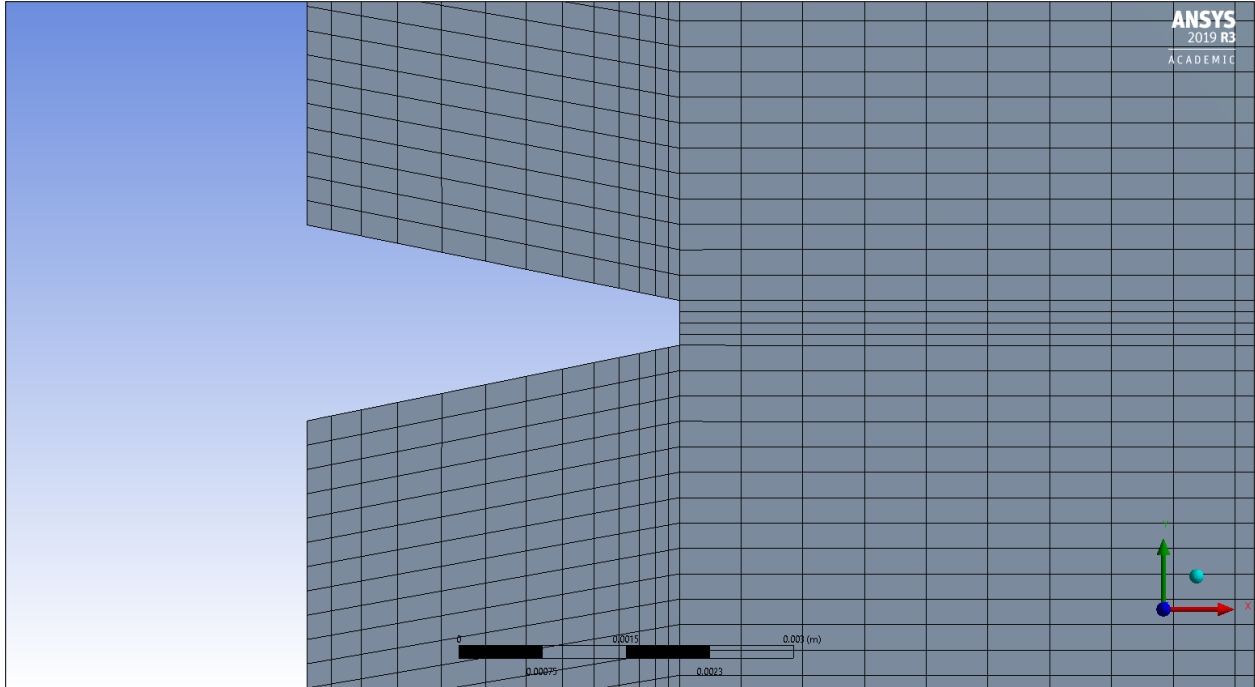


Figure 2.8: Closeup of individual fuel injector

The number of elements for the three-injector mesh increased to 637,134 elements. The increase in element size was needed for the resolution required to capture smaller inlets for the air and Hydrogen. If the element sizing near the inlets is too large, then ANSYS Fluent could treat it as a reversed flow even if the inlets are properly sized.

Table 2.5: Mesh quality metrics for three-injector mesh

Minimum Orthogonal Quality	0.96901
Maximum Skewness	0.15956
Maximum Aspect Ratio	6.6363

The mesh quality was also altered to account for the three fuel injectors. While the minimum orthogonal quality was reduced and the maximum skewness was increased, they were still within acceptable values regarding mesh quality. However, the aspect ratio increased which may lead to convergence issues because the individual elements became more elongated when the altered sizing was applied to the air and Hydrogen inlets.

2.2.1.3 Contoured Nozzle Mesh

The contoured nozzle was generated with the Method of Characteristics to eliminate the formation of oblique shockwaves in the nozzle section. The cross-sectional area of the combustion chamber was resized from (125 mm × 125 mm) to (70 mm × 70 mm) while the combustion chamber was kept at 305 mm.

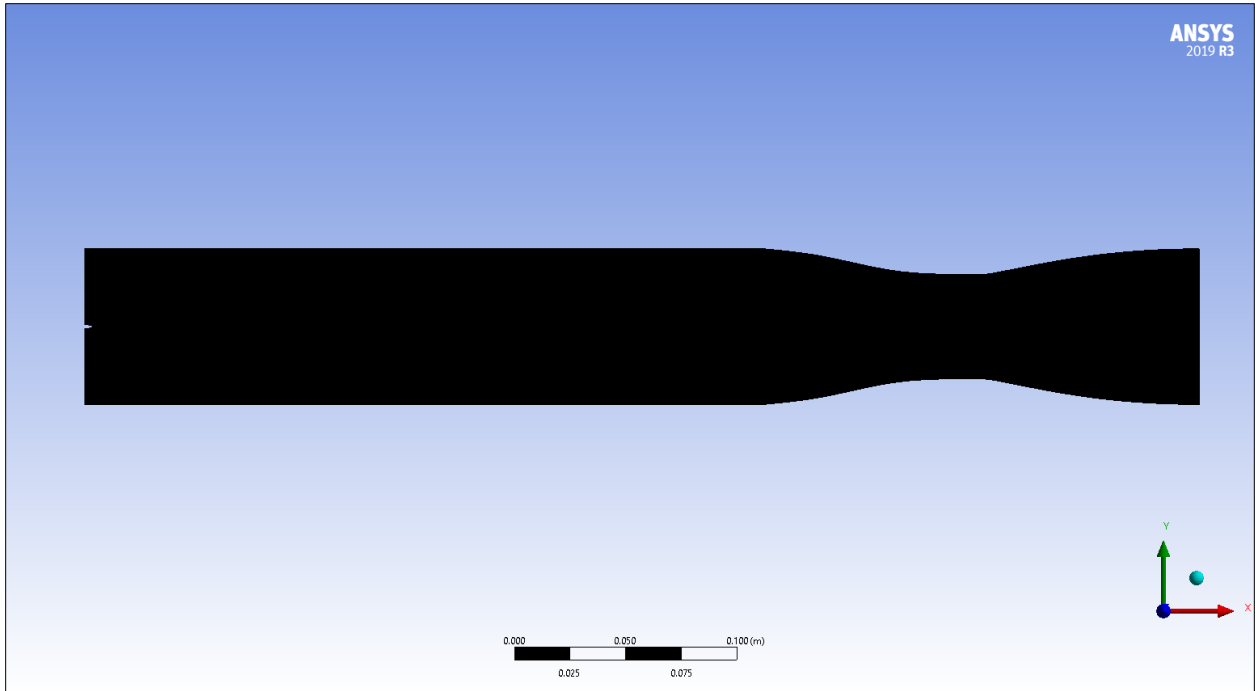


Figure 2.9: Mesh with contoured nozzle

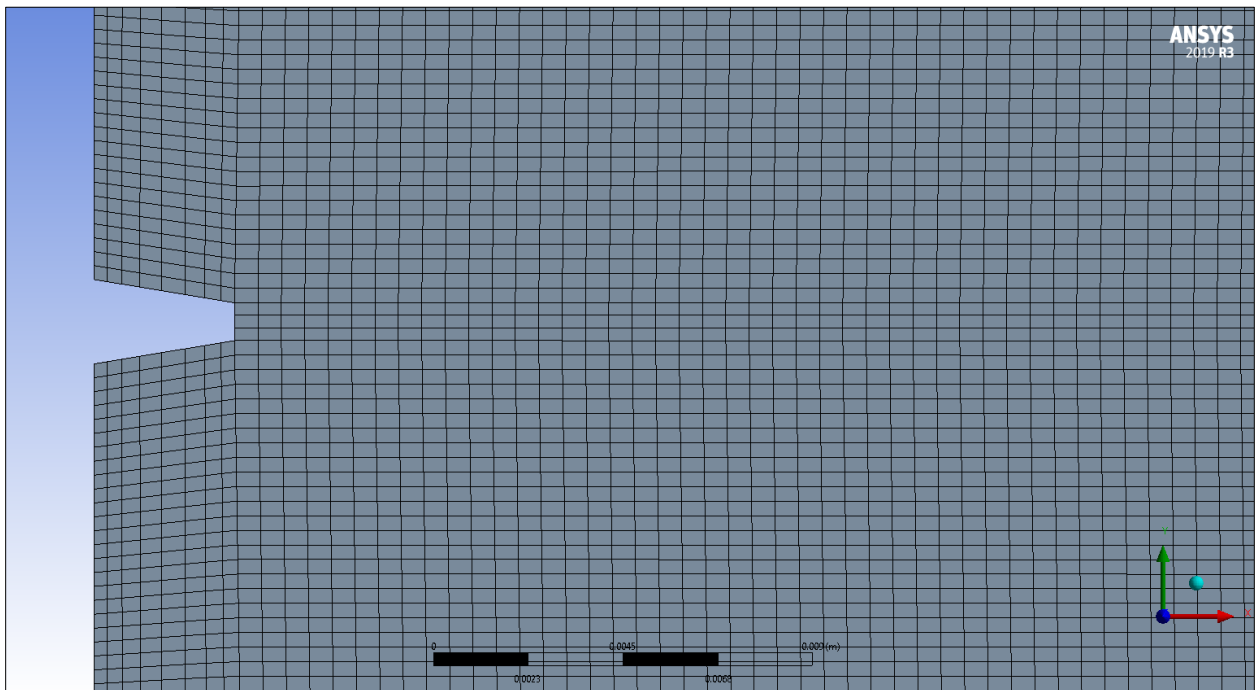


Figure 2.10: Fuel injector of contoured nozzle

The number of elements was reduced to 189,121 thanks to the reduced geometry size. While the minimum orthogonal quality and maximum skewness did not noticeable change, the maximum aspect ratio was greatly reduced to 4.232.

Table 2.6: Mesh quality metrics for contoured nozzle mesh

Minimum Orthogonal Quality	0.96773
Maximum Skewness	0.16295
Maximum Aspect Ratio	4.232

Table 2.7: Revised geometry for contoured nozzle mesh

Geometry Height (mm)	70
Combustion Chamber Length (mm)	305

2.2.1.4 Structured Axisymmetric Mesh

The single and three-injector layouts were still not producing adequate combustion which is why a new configuration with 17 injectors from the top to the bottom was implemented. The mesh was also done as an axisymmetric structured mesh with 70,400 elements and the axisymmetric nature of the mesh allowed for more resolution to be added in key sections of the mesh such as the walls of the combustion chamber and nozzle along with the nozzle throat.

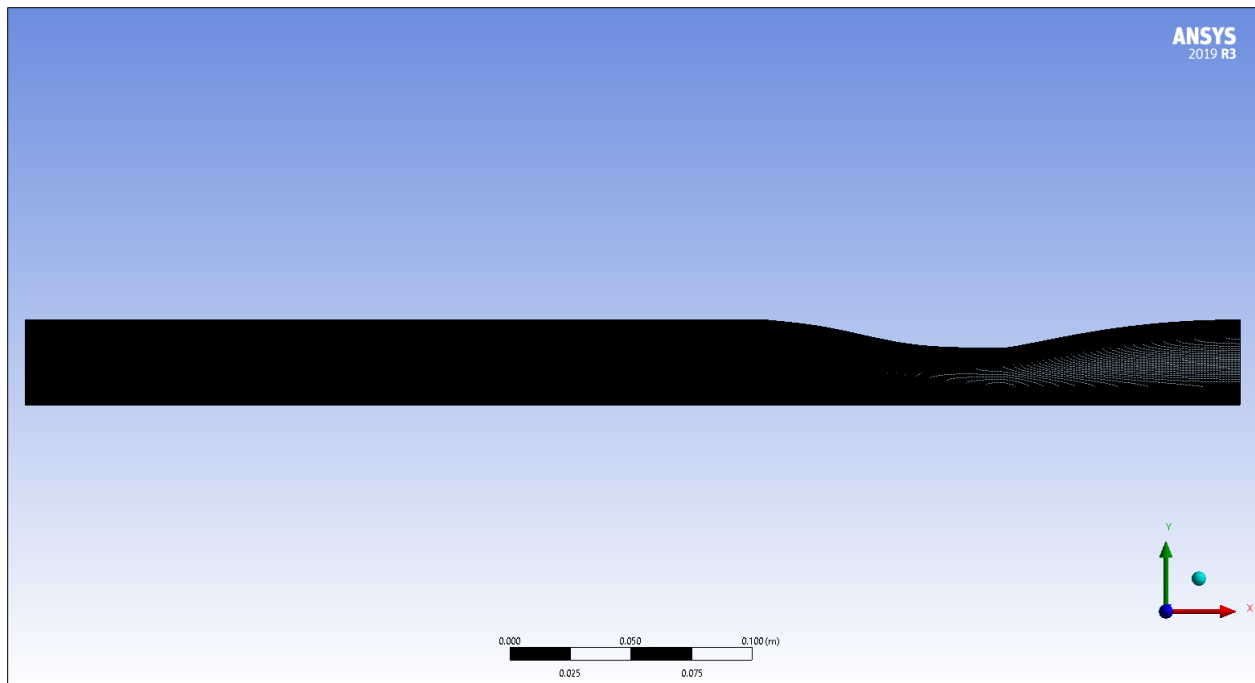


Figure 2.11: Structured axisymmetric mesh

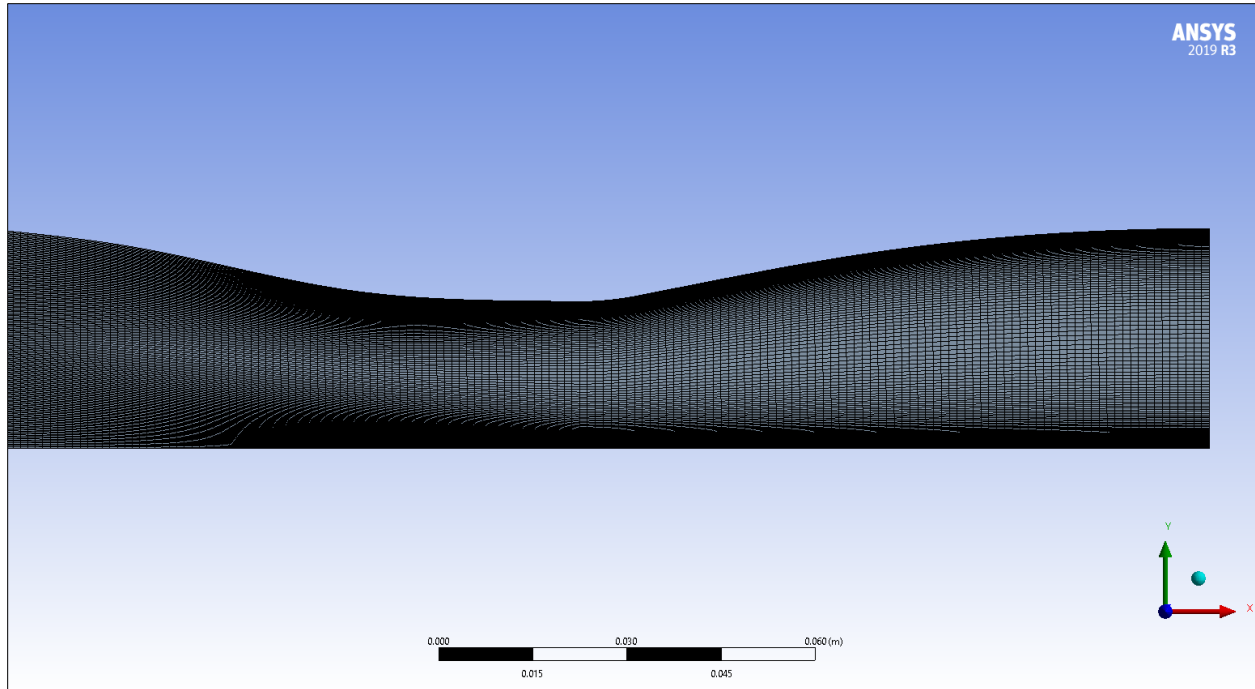


Figure 2.12: Meshing area around the nozzle of the structured axisymmetric mesh

Table 2.8: Mesh quality metrics for the structured axisymmetric mesh

Minimum Orthogonal Quality	0.53525
Maximum Skewness	0.14133
Maximum Aspect Ratio	74.826

While the updated mesh has provided improved combustion results, the mesh quality metrics have worsened. While skewness and orthogonal quality are still at adequate levels, the aspect ratio has become significantly higher than it was with the previous meshes. The geometry height and combustion chamber length used are the same values as the contoured nozzle mesh values in Table 2.7.

2.2.2 Current Mesh – Unstructured Axisymmetric Mesh

Due to the worsened aspect ratio from the structured axisymmetric mesh, an unstructured mesh was generated with to improve the mesh quality metrics as seen in Table 2.8. The aspect ratio is greatly lessened despite the increased skewness due to the unstructured nature of the mesh. The element size was also increased to 112,900 elements and the geometry height and combustion chamber length used were the same values as the contoured nozzle mesh values in Table 2.7.

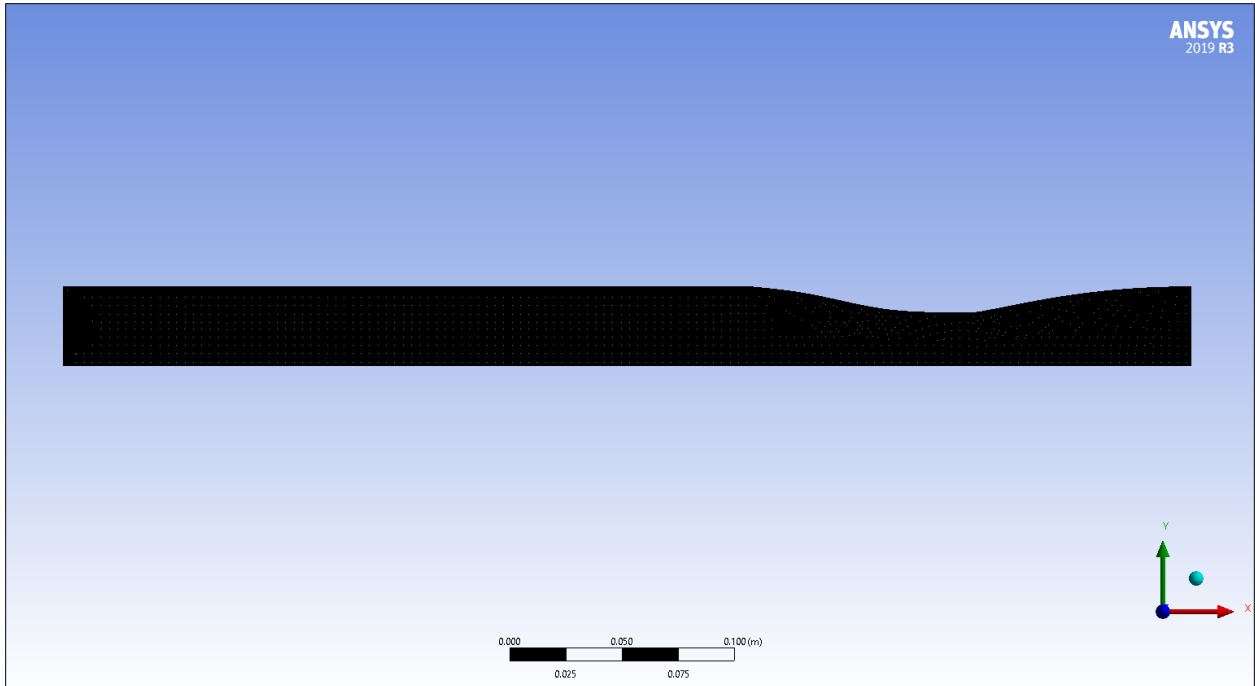


Figure 2.13: Unstructured axisymmetric mesh

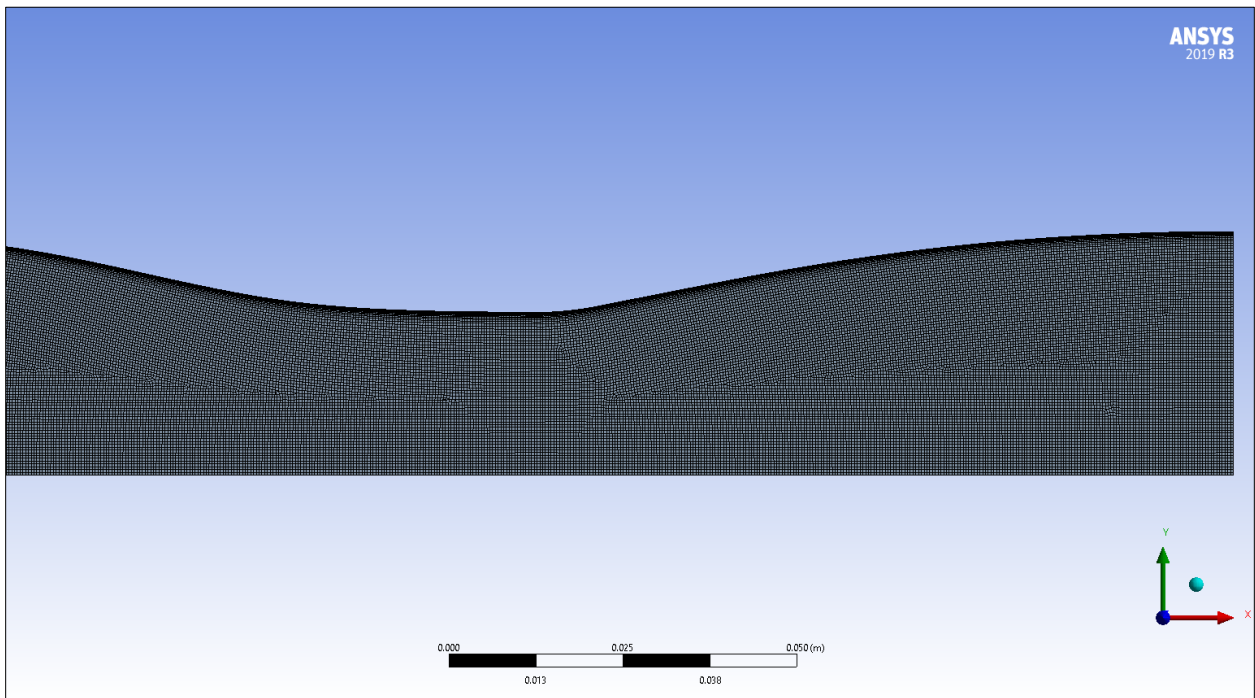


Figure 2.14: Meshing area around the nozzle of the unstructured axisymmetric mesh

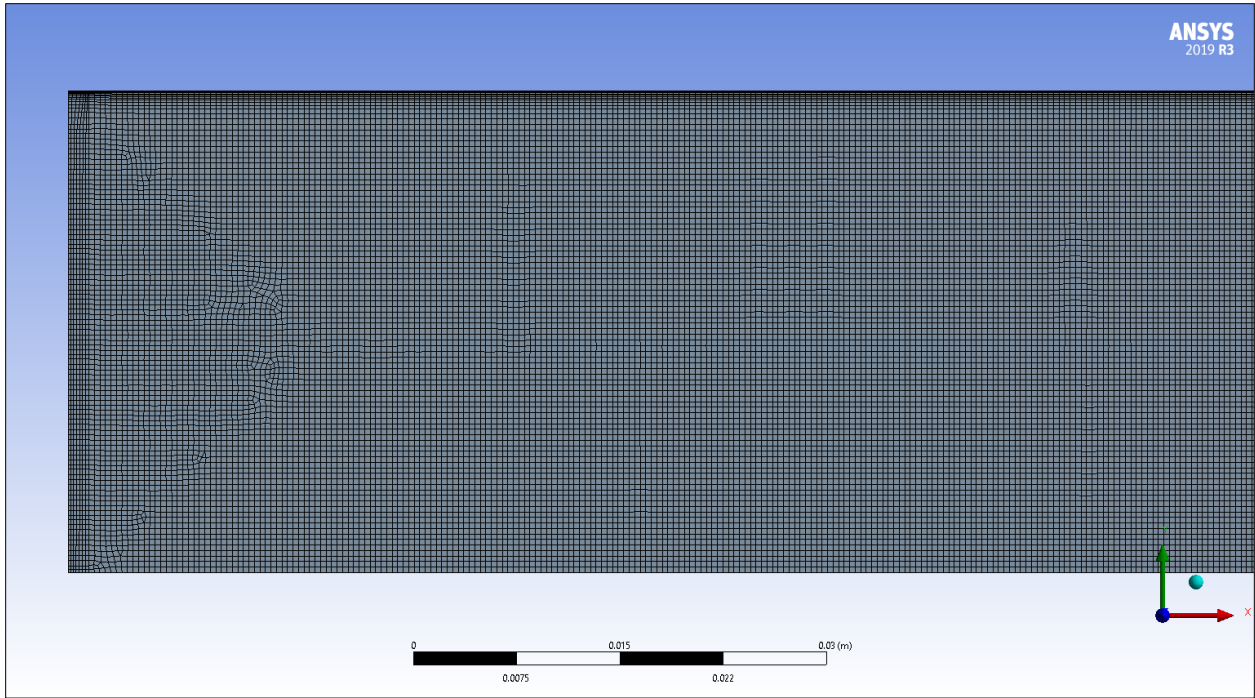


Figure 2.15: Meshing area around the inlet of the structured axisymmetric mesh

Table 2.9: Mesh quality metrics for the unstructured axisymmetric mesh

Minimum Orthogonal Quality	0.66207
Maximum Skewness	0.57378
Maximum Aspect Ratio	11.544

3. Boundary Conditions and Setup

3.1 Boundary Conditions for the Density-Based Solver

For the initial combustion chamber simulation, we needed to verify that our inputs at station 3 will result in the same conditions that were analytically computed for station 4 and station 10 as shown in Table 2.3 and Table 3.2. A steady-state model was utilized for the density-based setup.

For fuel injection, the gaseous Hydrogen fuel was originally planned to be provided by a series of injectors placed in the middle section shown in Figure 3.1 where a horizontal row of fuel injectors is placed at station 3. These fuel injectors would act as sonic nozzles for the Hydrogen fuel. The two larger blocks would be modeled as two air inlets with inputs from Table 3.1.

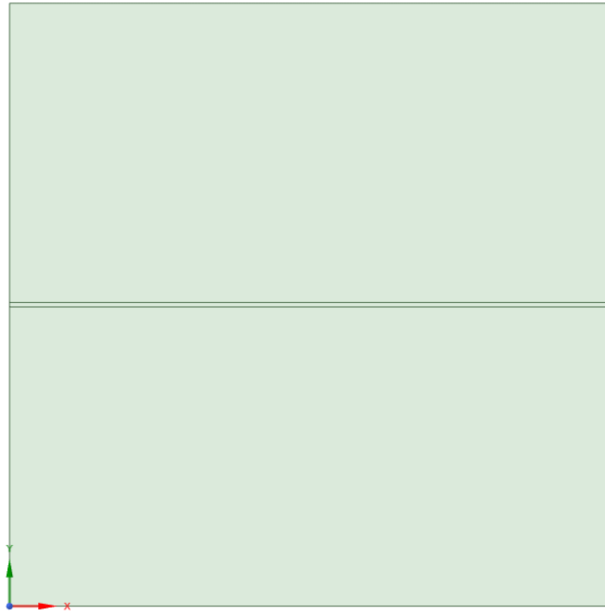


Figure 3.1: Cross sectional area of combustion chamber

Table 3.1: Station 3 air inlet conditions [15]

M_3	0.217
P_3 (kPa)	336.48
T_3 (K)	593.93
$T_{0,3}$ (K)	600

Table 3.2: Station 4 conditions [15]

M_4	0.435
P_4 (kPa)	274.71
T_4 (K)	1574.56
γ_4	1.283

For the station 3 air inlet conditions, we treated the region as an isentropic flow before Hydrogen is mixed in for combustion which allows us to use isentropic relations (3.1) to determine our total and static temperature and pressure values to establish our boundary conditions in ANSYS Fluent [17]. We also treated Hydrogen as a choked throat flow due to the choked fuel injectors to find our choked area from the Hydrogen mass flow rate of 0.038 kg/s.

$$\begin{aligned}\frac{T_0}{T} &= 1 + \frac{\gamma - 1}{2} M^2 \\ \frac{p_0}{p} &= \left(1 + \frac{\gamma - 1}{2} M^2\right)^{\gamma/(\gamma-1)} \\ \frac{\rho_0}{\rho} &= \left(1 + \frac{\gamma - 1}{2} M^2\right)^{1/(\gamma-1)}\end{aligned}\quad (3.1)$$

$$\dot{m} = \frac{p_0 A^*}{\sqrt{T_0}} \sqrt{\frac{\gamma}{R} \left(\frac{2}{\gamma + 1}\right)^{(\gamma+1)/(\gamma-1)}}\quad (3.2)$$

For Hydrogen, we assumed that γ for Hydrogen is 1.4 for a diatomic gas. We can then solve the equation in (3.2) for the choked area of our fuel injectors. With $A^* = L_{width} \times L_{height}$

Table 3.3: Injector throat dimensions

A (mm^2)	112
L_{width} (mm)	125
L_{height} (mm)	0.896

Table 3.4: Hydrogen inlet conditions [15]

M_{H_2}	1
P_{0,H_2} (kPa)	551.581
P_{H_2} (kPa)	290.862
T_{0,H_2} (K)	300
γ_{H_2}	1.4
\dot{m} (kg/s)	0.038

For the total pressure of the injector, we experimented with setting it to 80 psi or 551.581 kPa with the flow interaction being treated as a non-premixed flow. Because air and Hydrogen will both be gaseous, there was no need to model the interaction as a multiphase flow.

A mass flow inlet was initially chosen for both the air inlet and Hydrogen inlets; however, pressure inlets were used later due to ANSYS Fluent not modeling mass flow inlets as desired. A mass flow outlet was used for the station 4 exit of the combustion chamber; however, the outlet conditions were changed to reflect the nozzle exit conditions as a pressure outlet as seen in Table 2.3.

Our solver was set to density-based due to compressible flow conditions. We also set the Energy Equation to “On” and the viscosity model to SST k-omega due to its viability for this type of flow [4, 6]. Species Transport was used to model combustion with a separate air inlet and hydrogen injector. The settings can be seen in Figure 3.2.

Model

- Off
- Species Transport
- Non-Premixed Combustion
- Premixed Combustion
- Partially Premixed Combustion
- Composition PDF Transport

Reactions

- Volumetric
- Particle Surface

Chemistry Solver

Relax to Chemical Equilibrium

Integration Parameters...

Options

- Inlet Diffusion
- Full Multicomponent Diffusion
- Thermal Diffusion

Mixture Properties

Mixture Material: hydrogen-air [Edit...]

Import CHEMKIN Mechanism...

Number of Volumetric Species: 4

Turbulence-Chemistry Interaction

- Finite-Rate/No TCI
- Finite-Rate/Eddy-Dissipation
- Eddy-Dissipation
- Eddy-Dissipation Concept

Coal Calculator...

Options

Flow Iterations per Chemistry Update: 1

Aggressiveness Factor: 0.5

Temperature Threshold (K): 200

Select Boundary Species

Select Reported Residuals

Figure 3.2: Species transport settings

The reactions were set to volumetric, and the chemistry solver was set to relax to chemical equilibrium because the preliminary analytical simulations were done with chemical equilibrium in mind. The default Hydrogen-Air mixture was used for the CHEMKIN settings within the species transport settings.

Table 3.5: Property settings for air inlet

Density	Ideal Gas
C_p	Kinetic Theory
Thermal Conductivity	Kinetic Theory
Viscosity	Kinetic Theory

Because the flow is combusting, properties such as specific heat, thermal conductivity and viscosity cannot be set to constant values which is the default setting for ANSYS Fluent. Instead, Kinetic Theory settings must be implemented to take in account for the variable nature of fluid properties during combustion. The Hydrogen-Air mixture properties and the properties for the materials that are being mixed have been altered from the previous progress report. Due to the flow combustion that is present, specific heat, thermal conductivity, and viscosity will not be

constant, instead they will need to be treated as variables that will be calculated for by ANSYS Fluent.

Table 3.6: Property settings for hydrogen-air mixture

Density	Ideal Gas
C_p	Mixing Law
Thermal Conductivity	Ideal Gas Mixing Law
Viscosity	Ideal Gas Mixing Law

The settings for the materials that make up the mixture (Hydrogen, Oxygen, Water-Vapor, Nitrogen) will also need to be changed for the combustion flow.

Table 3.7: Property settings for individual elements at inlet

C_p	Piecewise Polynomial
Thermal Conductivity	Kinetic Theory
Viscosity	Kinetic Theory

Implicit formulation was used to allow for faster calculations with the spatial discretization settings specified in Table 3.8. Third Order MUSCL (Monotone Upstream-Centered Scheme) was used for spatial discretization settings for increased spatial accuracy [4].

Table 3.8: Spatial discretization settings for density-based solver

Gradient	Least Squares Cell Based
Flux Type	AUSM
Flow	Third Order MUSCL
Turbulent Kinetic Energy	Third Order MUSCL
Specific Dissipation Rate	Third Order MUSCL

3.1.1 Boundary Conditions for the Three Fuel Injectors Layout

For the three-injector layout, the throat dimensions of each Hydrogen fuel inlet were altered to take in account the different mass flow rate that would come out of each individual injector.

Table 3.9: Individual injector dimensions in three-injector layout

A (mm^2)	37
L_{width} (mm)	125
L_{height} (mm)	0.296

The inlet conditions for the individual injectors remain unchanged aside from the mass flow rate being 1/3 of the mass flow rate from Table 3.4.

Table 3.10: Individual injector conditions in three-injector layout

M_{H_2}	1
P_{0,H_2} (kPa)	551.581
P_{H_2} (kPa)	290.862
T_{0,H_2} (K)	300
γ_{H_2}	1.4
\dot{m} (kg/s)	0.012667

3.2 Boundary Conditions for the Pressure-Based Solver

Due to time constraints and because the density-based solver was still not achieving our desired results, we then opted to investigate the non-premixed combustion model since it is a simpler combustion model to implement than the Species Transport model. However, the non-premixed combustion model is not available in the density-based solver for ANSYS Fluent which is why the pressure-based solver was implemented for this case.

For fuel injection, the gaseous Hydrogen fuel will be provided by a series of 17 injectors placed vertically from the top to bottom as shown in Figure 3.3 where a vertical row of fuel injectors is placed at station 3 while Table 3.11 shows the revised injector area.

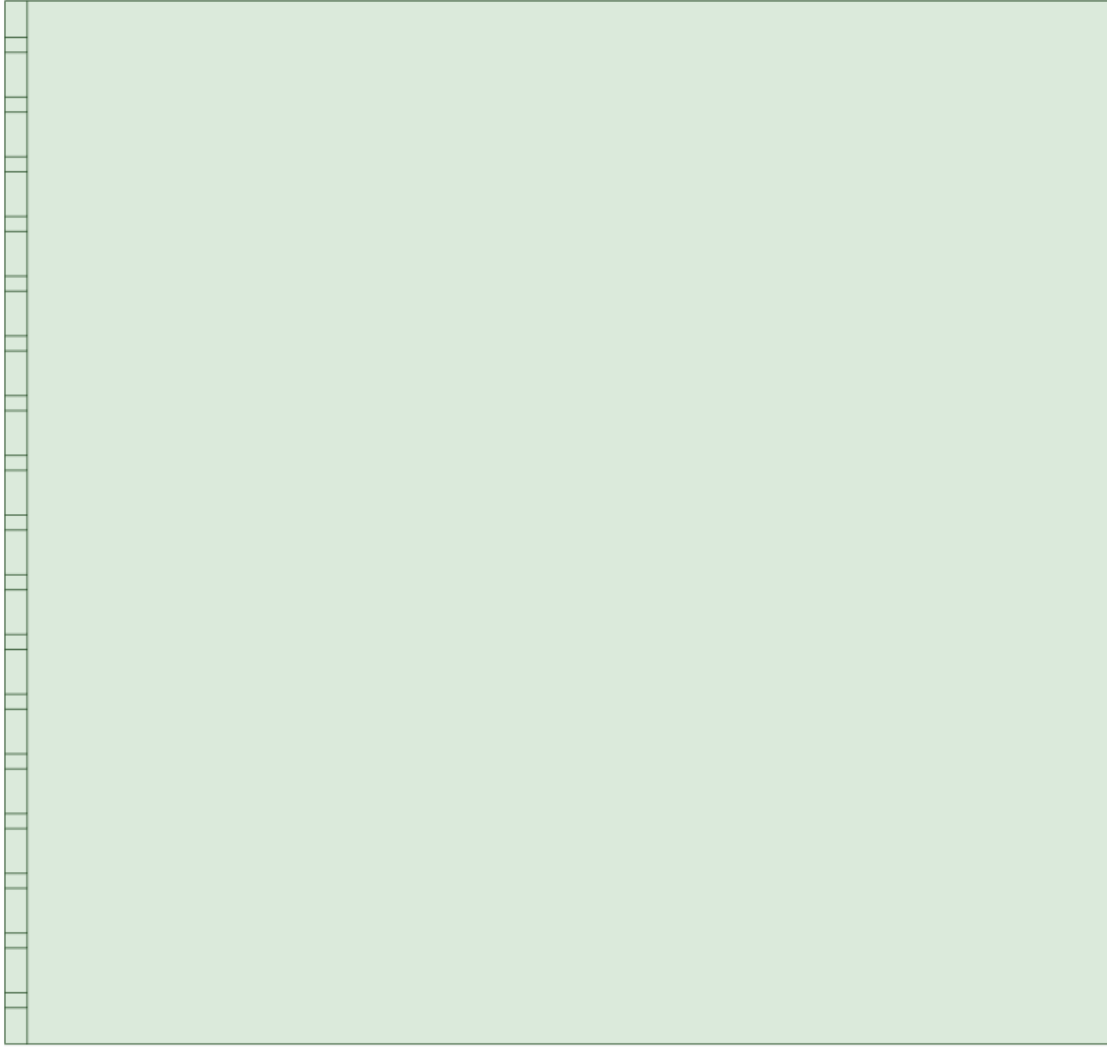


Figure 3.3: Injector geometry

Table 3.11: Revised injector area

Combined Injector Area (mm^2)	1190
Height of Individual Injectors (mm)	1

Table 3.12: Mass flow rates used for air and fuel mass flow inlets [15]

\dot{m}_{fuel} (kg/s)	0.038
\dot{m}_{air} (kg/s)	3.28

A mass flow inlet was chosen for both the air inlet and Hydrogen inlets with a pressure-based outlet for the nozzle exit. Our solver is set to pressure-based to allow for the usage of non-premixed combustion for our combustion model. We have also set the Energy Equation to “On” and the viscosity model to SST k-omega due to its viability for this type of flow [4, 6].

The PDF settings for non-premixed combustion had inlet diffusion and compressibility effects selected for increased accuracy along with a steady diffusion flamelet. The CHEMKIN Mechanism used was GRI-Mech 3.0 from UC Berkeley’s Combustion Lab [19]. The species mole fractions are shown in Table 3.13. The equilibrium operating pressure for the non-premixed combustion model was set to 305,595 Pa since it’s the average static pressure within the combustion chamber.

Table 3.13: Mole fractions

H_2	1
O_2	0.21008
N_2	0.78992

Implicit formulation was used to allow for faster calculations with the spatial discretization settings specified in Table 3.14. The number of time steps will vary depending on how long we want to run the simulation for. A transient model was utilized since certain propulsion processes such as ignition are unsteady phenomena that need to be treated as transient processes [21].

Table 3.14: Spatial discretization settings for pressure-based solver

Pressure-Velocity Coupling Scheme	SIMPLE
Gradient	Least Squares Cell Based
Pressure	Second Order
Density	Second Order Upwind
Turbulent Kinetic Energy	Second Order Upwind
Specific Dissipation Rate	Second Order Upwind
Energy	Second Order Upwind
Mean Mixture Fraction	Second Order Upwind
Mixture Fraction Variance	Second Order Upwind
Transient Formulation	First Order Implicit

Table 3.15: Transient calculation parameters

Time Step Size (s)	0.0001 and 0.00001
Number of Time Steps	Varies
Max Iterations/Time Step	60

The pressure-based simulation does not allow for a 0 Pa operating pressure. Due to this we used a mean flow pressure of 222.22 kPa as our operating pressure with our mean flow pressure being the averaged static pressure across our simulated geometry (station 3, station 4, and the outlet) from Table 2.3, Table 3.1, and Table 3.2. This could result in negative pressure values in ANSYS Fluent’s static pressure contours and solution plots since the operating pressure is higher than our outlet static pressure of 55.47 kPa.

4. Results and Discussion

4.1 Preliminary Results

4.1.1 Generic Nozzle

Figures 4.1 to 4.6 show our unconverged results thus far for the original generic nozzle mesh that was used.

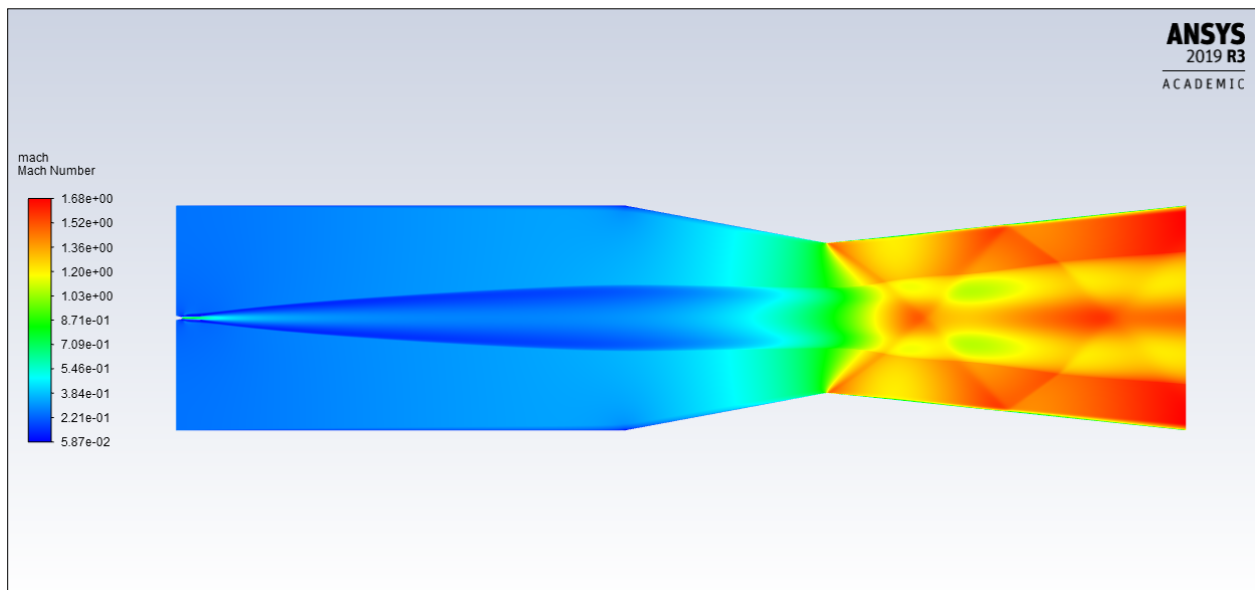


Figure 4.1: Mach contours for the generic nozzle

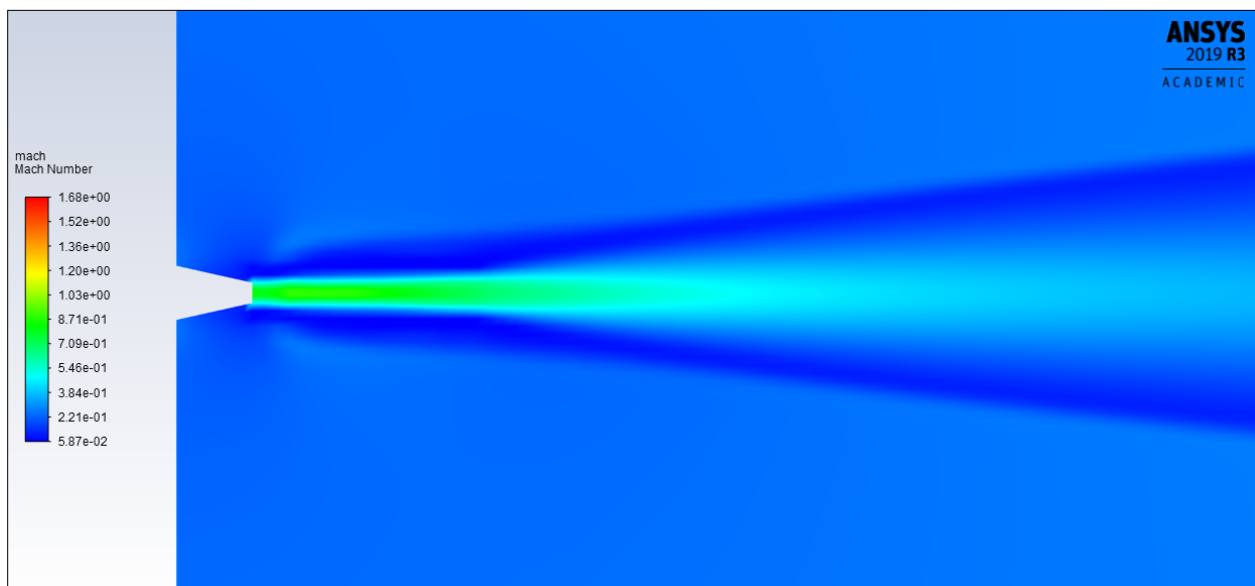


Figure 4.2: Mach contours near fuel injector for the generic nozzle

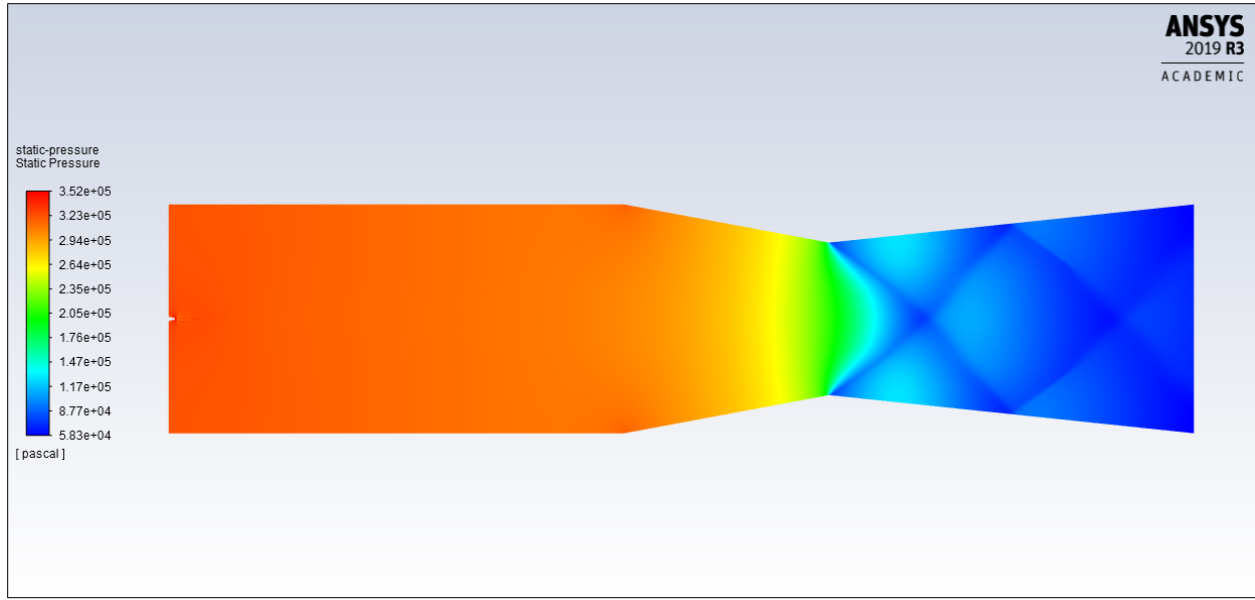


Figure 4.3: Static pressure contours for the generic nozzle

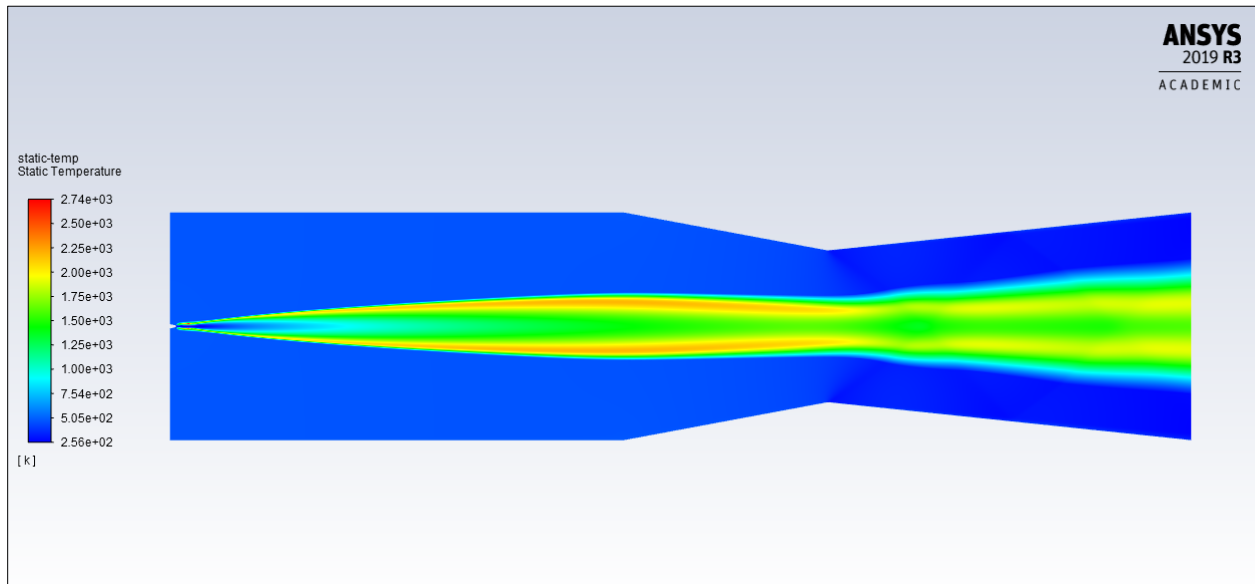


Figure 4.4: Static temperature contours for the generic nozzle

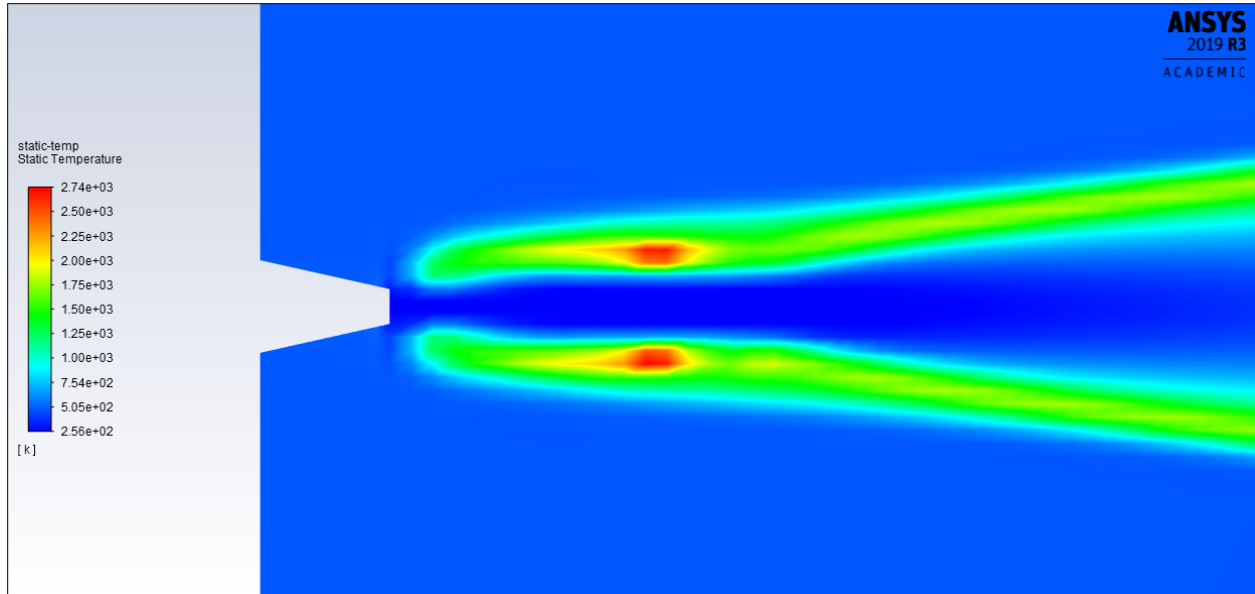


Figure 4.5: Static temperature contours near fuel injector for the generic nozzle

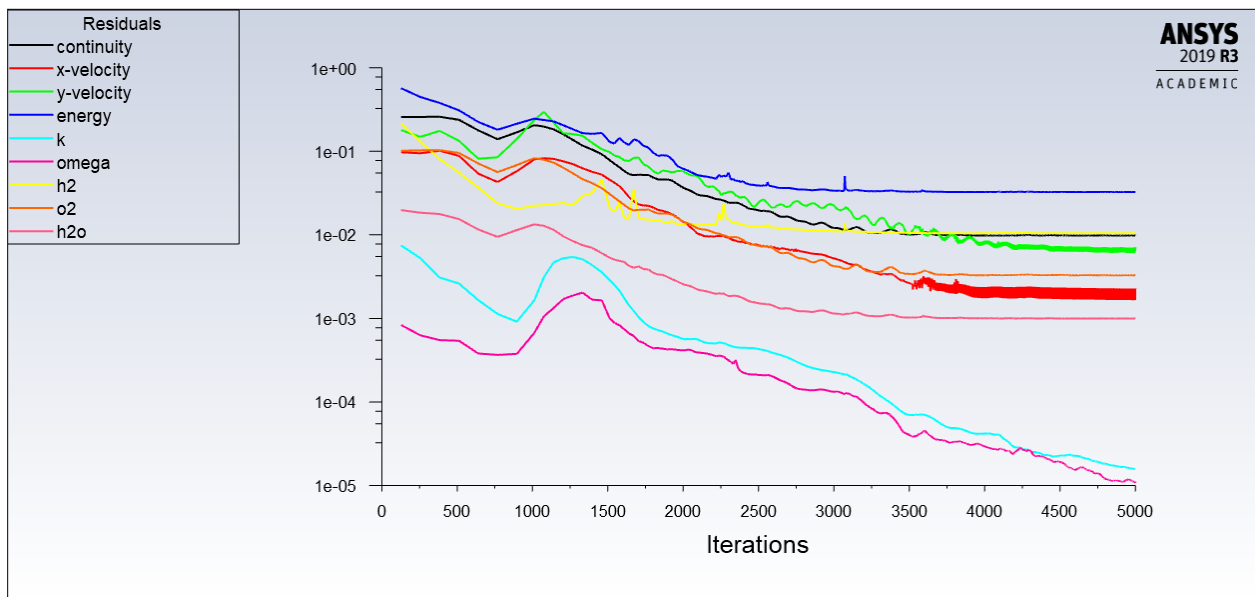


Figure 4.6: Residuals for the generic nozzle

According to Table 4.1, it appears that our Mach number at the exit is 1.514 instead of 1.806 as was found in the analytical simulations. The static pressure at the exit is also higher at 77.74 kPa instead of the 55.47 kPa which was found analytically. Our static temperature is also lower at 977.28 K instead of 1106.68 K. We can see that oblique shockwaves are present in the divergent nozzle section in Figure 4.3 with the resultant wave drag likely causing the difference in outlet conditions.

Table 4.1: Comparison of outlet conditions for the generic nozzle

	Expected Outlet Conditions	Area Weighted Average in Simulated Outlet
M_{10}	1.806	1.514
P_{10} (kPa)	55.47	77.74
T_{10} (K)	1106.68	977.28

While combustion does occur, complete combustion does not occur, and the resulting area weighted average temperatures are not as high as the temperatures that were found in the analytical simulations as seen in Table 2.3 and Table 3.2. The Hydrogen fuel plume from the injector is also narrow which points to insufficient turbulent mixing and would explain for the reduced temperatures. Judging by the contours from Figure 4.4, it appears that the current fuel injector plume only takes up about 1/3 of the combustion chamber at station 4.

4.1.2 Three Fuel Injectors

To improve the amount of turbulent mixing that is occurring the injector layout was changed to use three fuel injectors instead of one as seen in Figure 2.7. The dimensions of the fuel injectors were also changed to maintain an overall mass flow rate of 0.038 kg/s from all three fuel injectors.

Despite the increase in turbulent mixing, the three-injector layout has not converged. Instead, we note that the simulation sharply diverges when we use the values from Table 3.12 and Table 3.13. The only three-injector simulation that did not diverge sharply was when the individual injectors were given the same dimensions and boundary conditions as the initial single-injector layout as seen in Table 3.3. and Table 3.4. The layout with injector throat sizing from the single-injector simulation was initially simulated with the total pressure adjusted to maintain our overall mass flow rate. This simulation also diverged instead of converging.

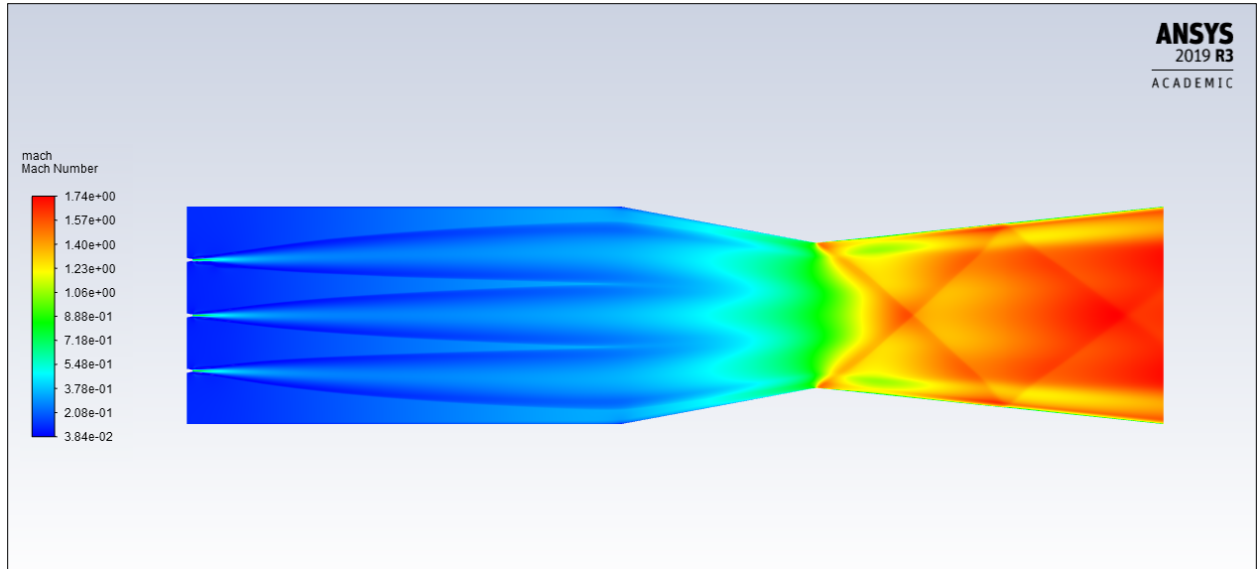


Figure 4.7: Mach contours for three-injector layout with original injector area

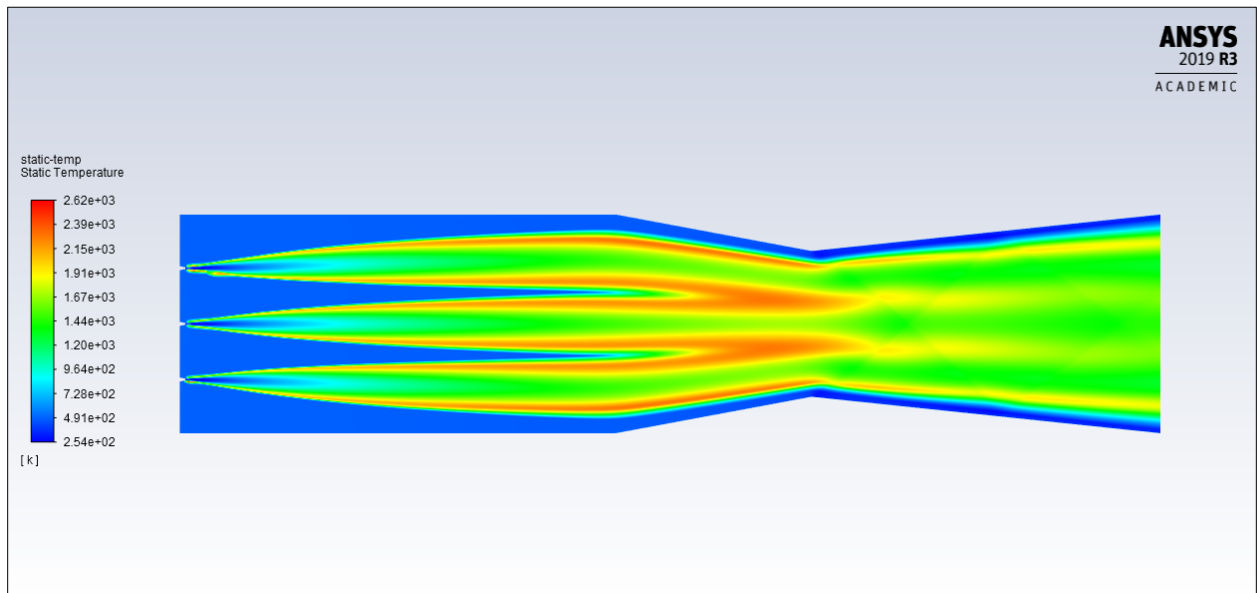


Figure 4.8: Static temperature contours for three-injector layout with original injector area

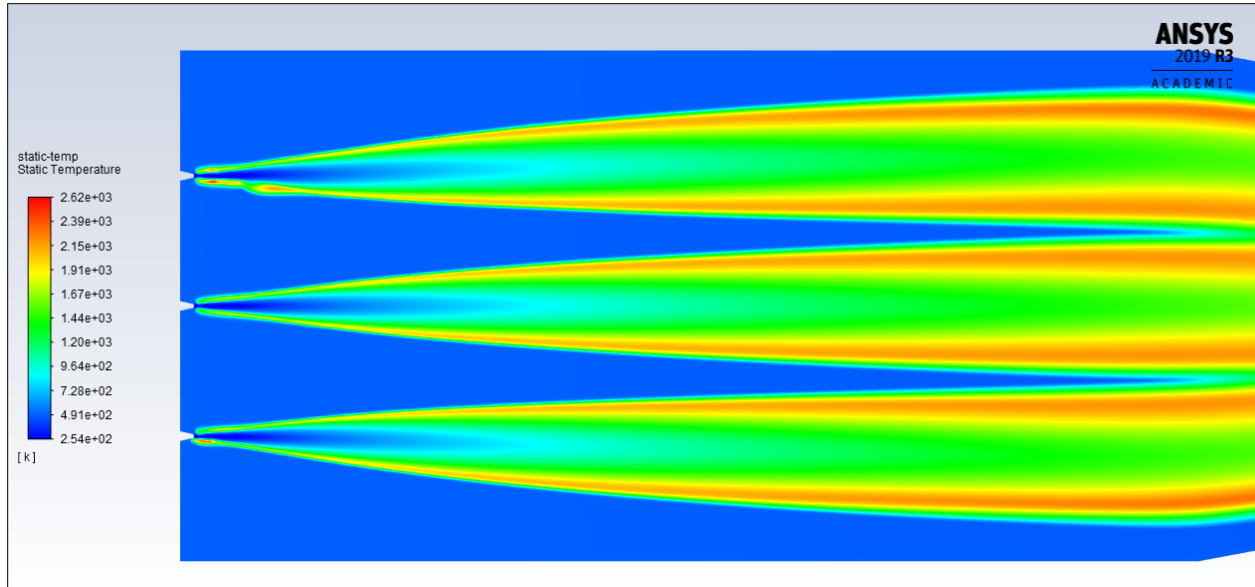


Figure 4.9: Closeup of static temperature contours for three-injector layout with original injector area

Figures 4.7 to 4.8 show the Mach and Static Temperature contours when the injectors are sized to the original dimensions and when the conditions are also the same as the original dimensions (Table 3.3 and Table 3.4) as the single-injector layout. Because the original conditions are being used with the original injector area, there is now three times more Hydrogen being injected. We can see that the overall temperatures are cooler than the single injector layout. However, this is to be expected due to the increased Hydrogen flow which results in an increased cooling effect.

The three-injector simulation with the mass flow adjusted initial conditions and dimensions are expected to look different from Figures 4.7 to 4.9. Namely with the expectation of combustion occurring solely within the combustion chamber instead of also occurring within the convergent section of the nozzle past station 4 as seen in Figure 4.4 and Figure 4.8. Combustion occurring within the convergent section could lead to less predictable flow and may be a contributor to our convergence issues.

4.1.3 Contoured Nozzle

A contoured nozzle was developed using the Method of Characteristics and the overall cross-sectional area was reduced to (70 mm × 70 mm) from the original (125 mm × 125 mm) height to allow for easier fuel mixing which showed improvements in combustion. As we can see in Figure 4.10, the contoured nozzle prevents the development of oblique shockwaves in the divergent section.

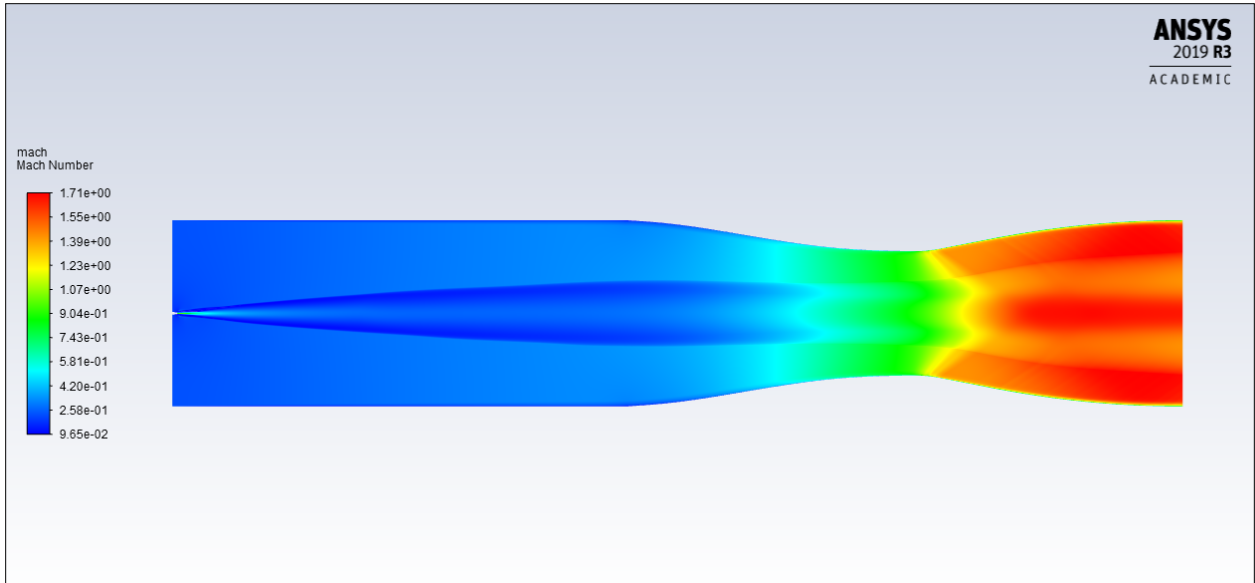


Figure 4.10: Mach contours for the contoured divergent nozzle

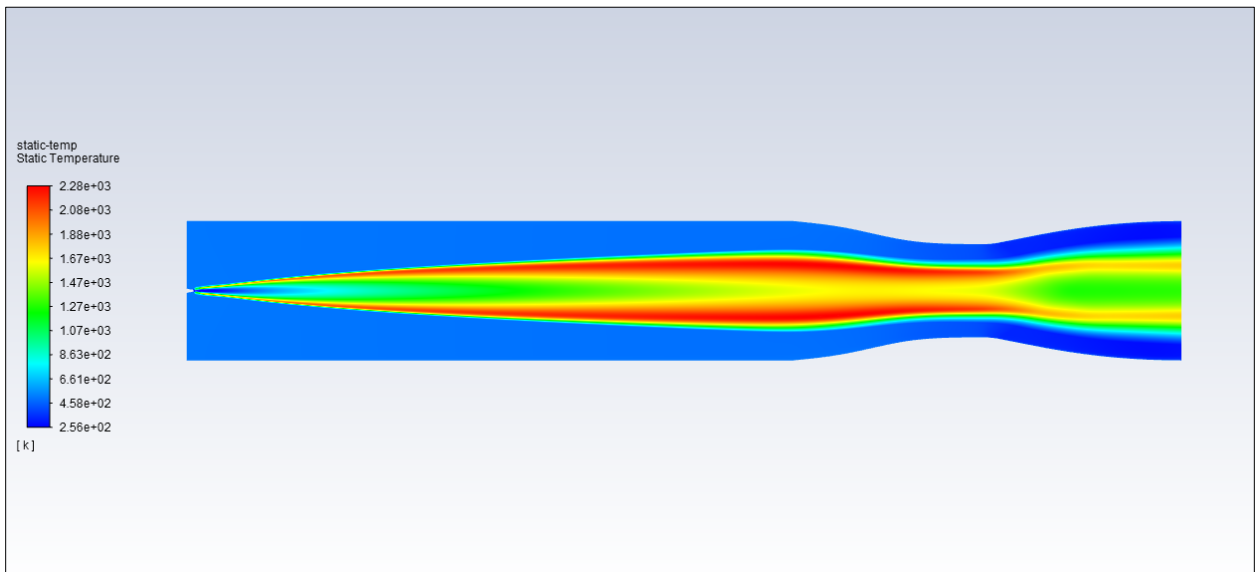


Figure 4.11: Static temperature contours for the contoured divergent nozzle

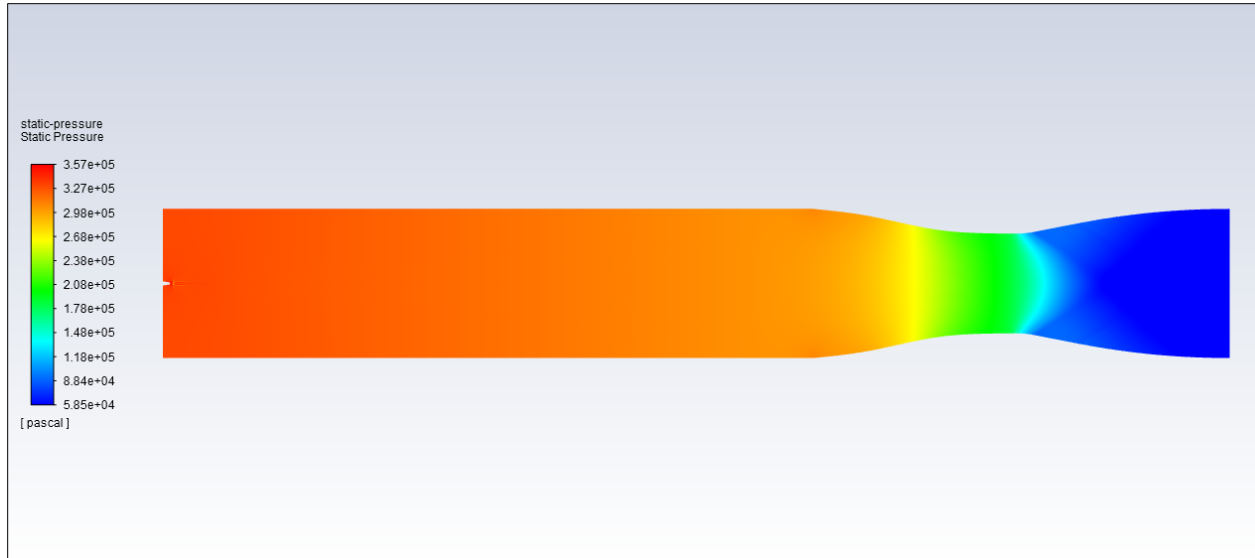


Figure 4.12: Static pressure contours for the contoured divergent nozzle

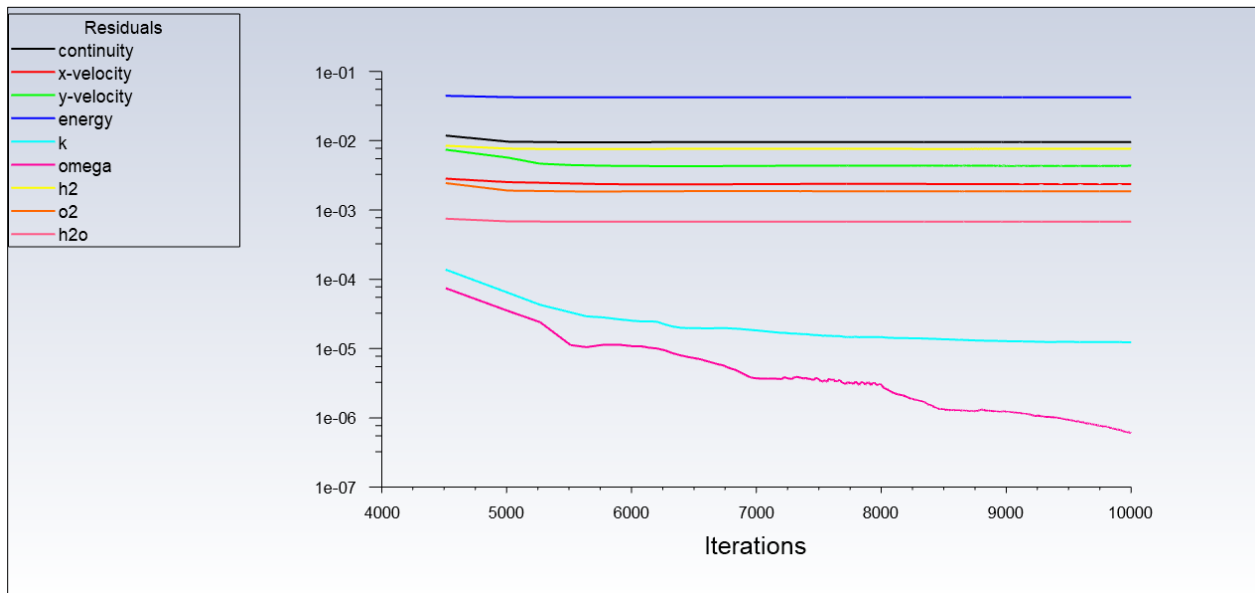


Figure 4.13: Residuals for the contoured divergent nozzle

Despite the contoured divergent nozzle being generated with no oblique shockwave formations in the nozzle, there is still a lack of convergence. Table 4.2 does show that the static temperature values match up closely while our Mach and static pressure values differ from our expected outlet conditions. The reduced Mach number at the outlet is likely due to viscosity losses from the boundary layer. Due to the lack of full combustion with the density-based solver and the species transport model, it was decided to switch to the pressure-based solver to utilize the non-premixed combustion model that's only available within ANSYS Fluent's pressure-based solver.

Table 4.2: Comparison of outlet conditions for the contoured nozzle

	Expected Outlet Conditions	Area Weighted Average in Simulated Outlet
M_{10}	1.806	1.602
P_{10} (kPa)	55.47	68.63
T_{10} (K)	1106.68	1088.66

4.1.4 Structured Axisymmetric Mesh

Our switch to a pressure-based solver with a non-premixed combustion species model and a transient simulation has produced promising results. The time step used was 0.0001.

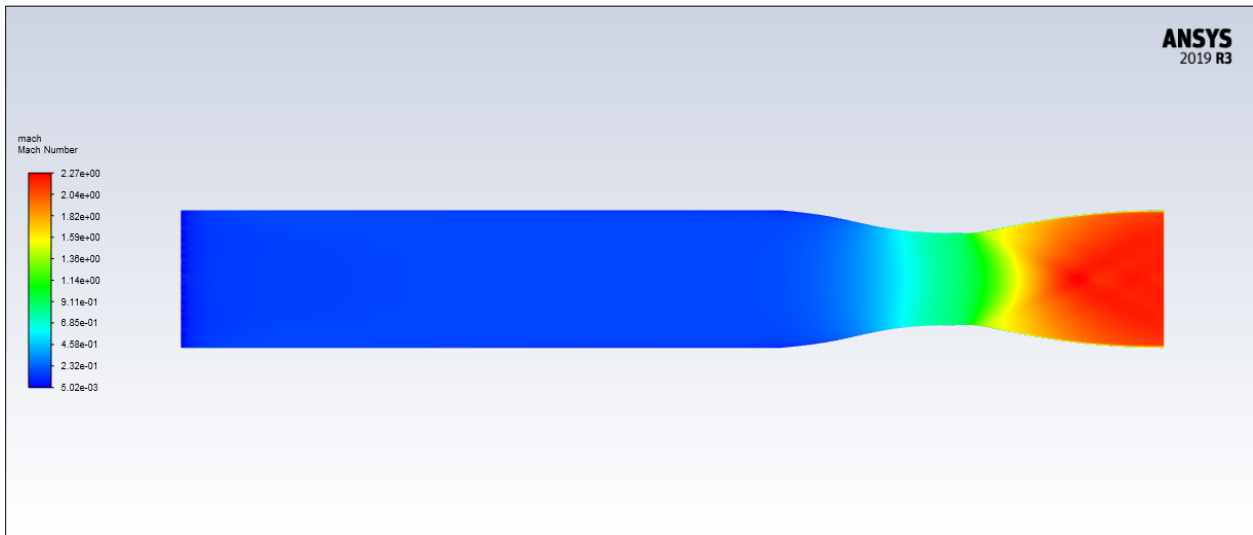


Figure 4.14: Mach contours for the structured axisymmetric mesh

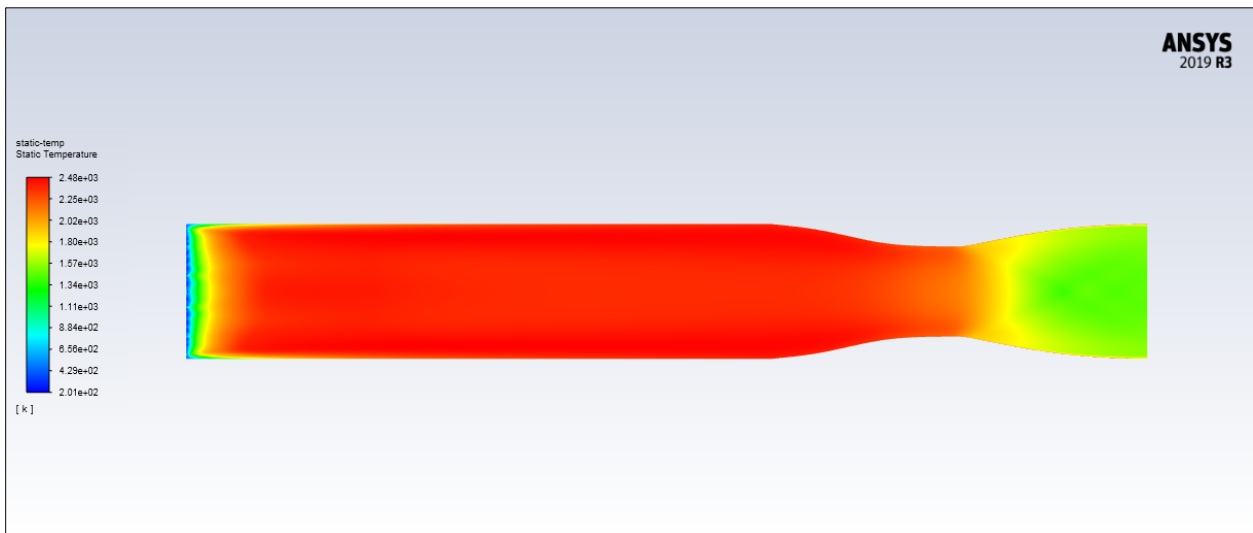


Figure 4.15: Static temperature contours for the structured axisymmetric mesh

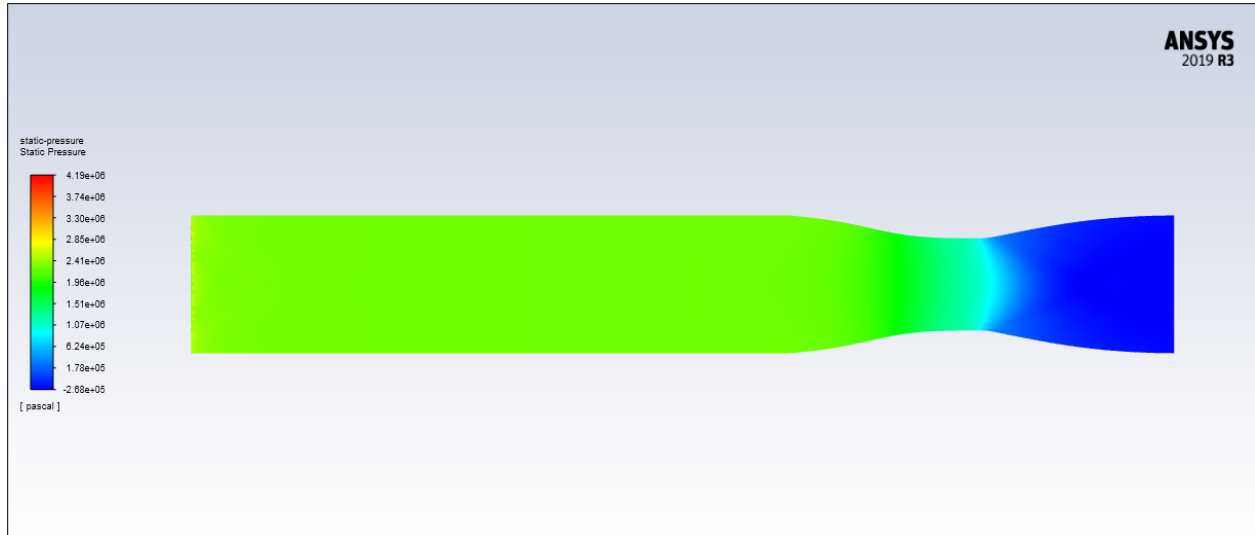


Figure 4.16: Static pressure contours for the structured axisymmetric mesh

Our updated contours are significantly improved over our previous set of contours with our static temperature contours behaving as expected. While the contours show improved combustion characteristics, there are some slight deviations from what we originally expected regarding the Mach number, static pressure, and static temperature at the outlet as shown in Table 4.3.

Table 4.3: Comparison of outlet conditions for the structured axisymmetric model

	Expected Outlet Conditions	Area Weighted Average in Simulated Outlet
M_{10}	1.806	2.129
P_{10} (kPa)	55.47	-35.71
T_{10} (K)	1106.68	1575.46

The static pressure contour plots are also interesting due to the large spike in static pressure towards the injectors, this could be due to our solution setup or because of a meshing issue. We also notice that the contours show negative pressure values towards the nozzle exit itself while the area-weighted average pressure was found to be a negative value as well.

This phenomenon can be attributed to the outputted static pressure contours and plots being relative to the operating pressure set for ANSYS Fluent instead of the absolute operating pressure, hence the negative values. Meanwhile, the density-based simulations allowed us to set the operating pressure to 0 Pa which allowed us to treat the outputted static pressure contours and plots as absolute values.

Due to the switch to a transient simulation, we also needed to monitor report plots for metrics such as the drag force along the walls or the area weighted Mach number towards the nozzle outlet. These are shown in Figures 4.17 – 4.22.

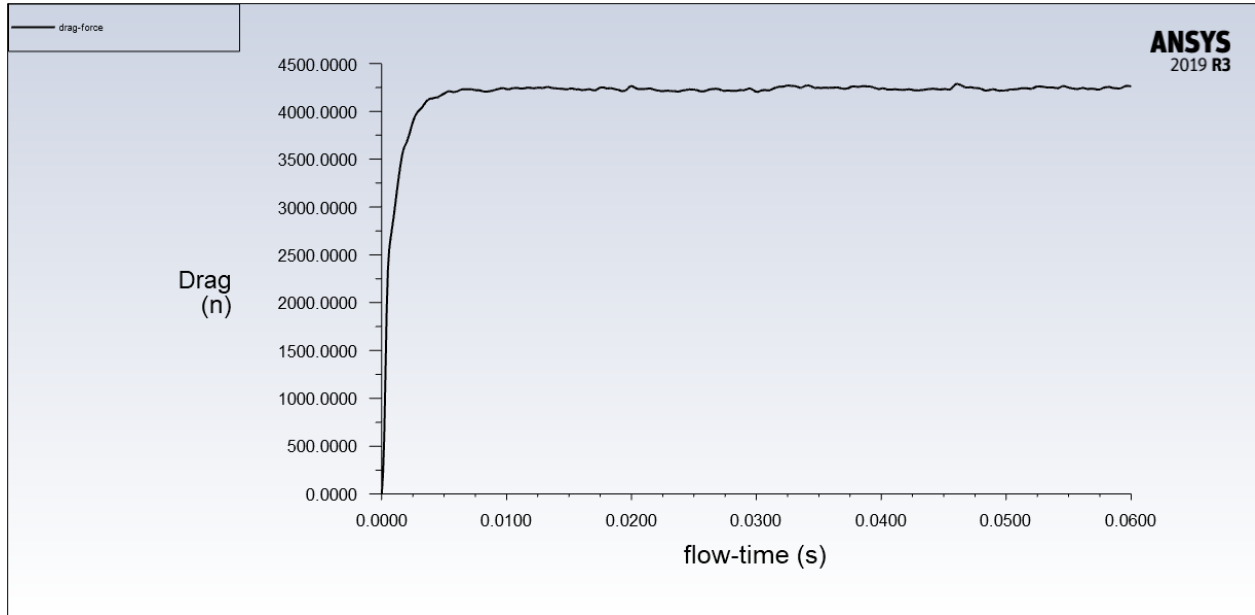


Figure 4.17: Drag force near walls for the structured axisymmetric mesh

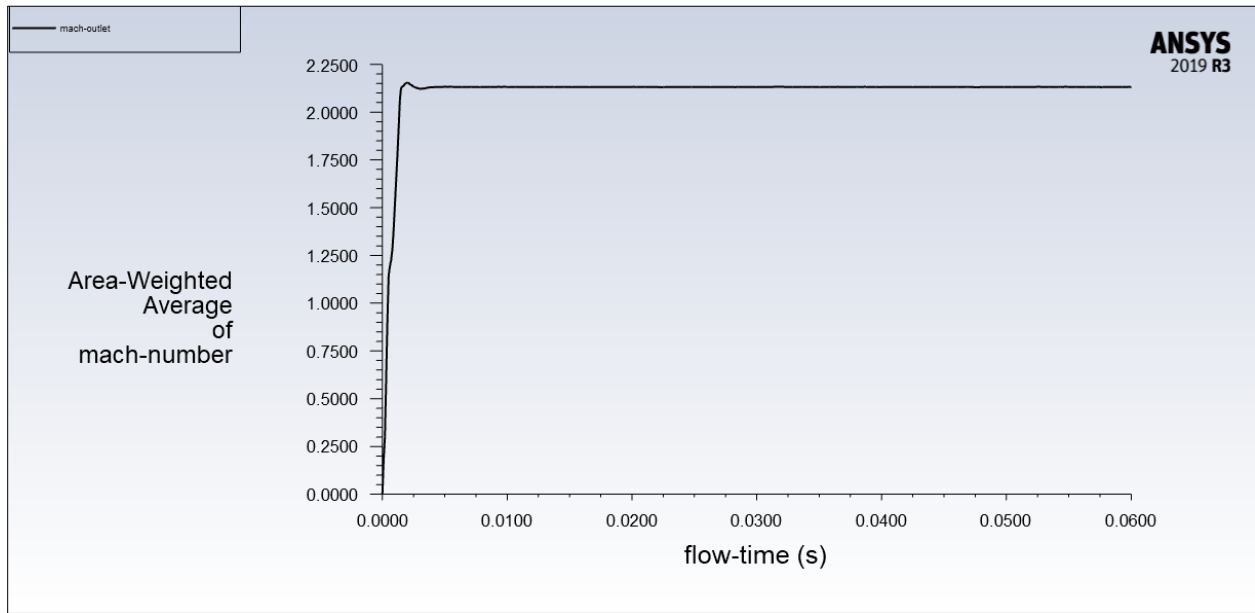


Figure 4.18: Area-weighted average of Mach number at the outlet for the structured axisymmetric mesh

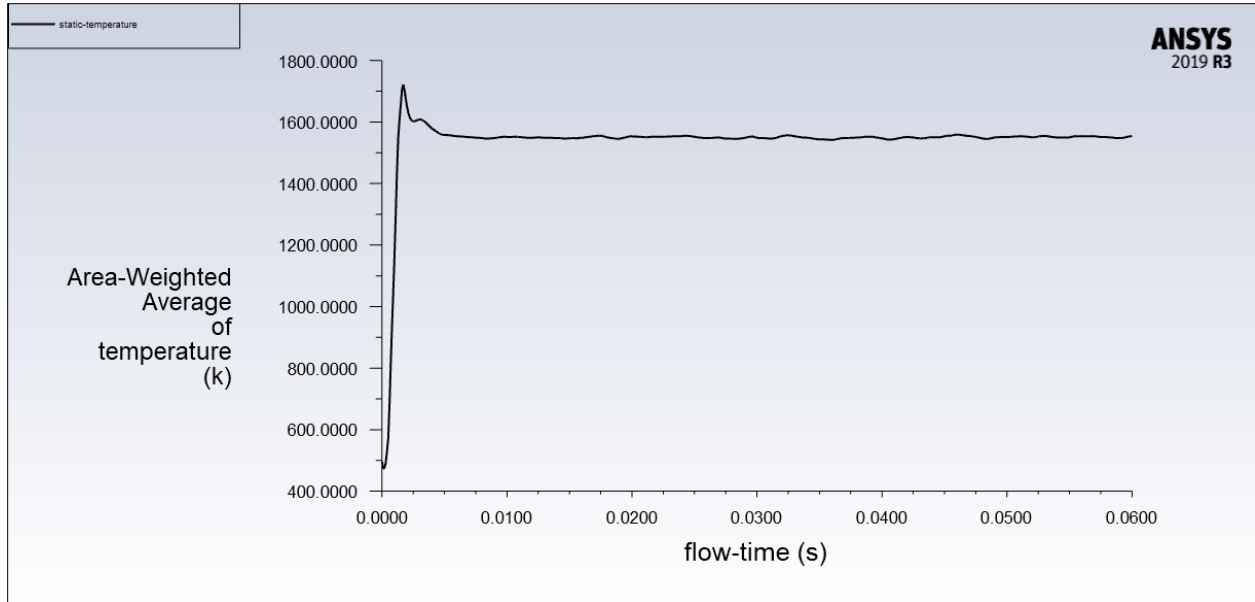


Figure 4.19: Area-weighted average of static temperature at the outlet for the structured axisymmetric mesh

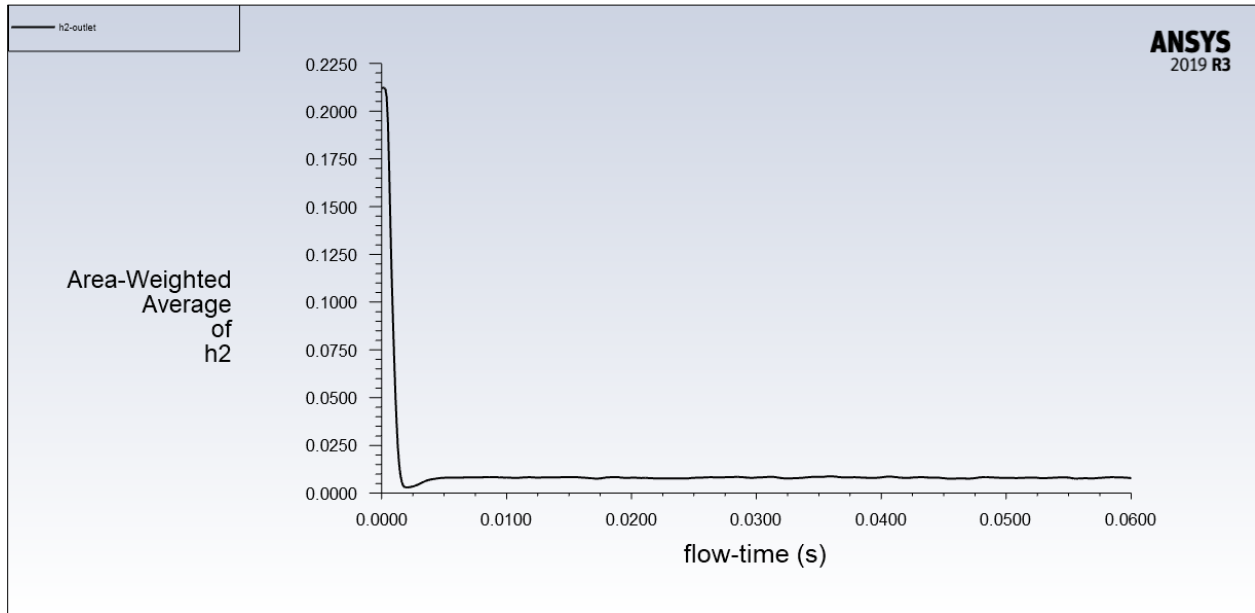


Figure 4.20: Area-weighted average of hydrogen at the outlet for the structured axisymmetric mesh

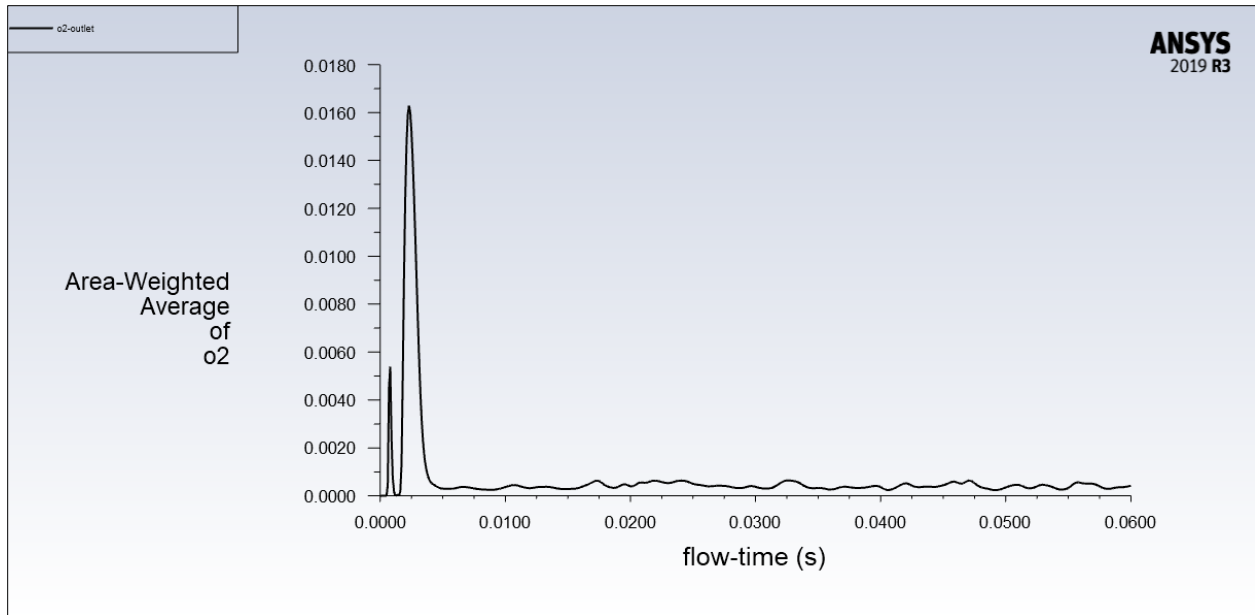


Figure 4.21: Area-weighted average of oxygen at the outlet for the structured axisymmetric mesh

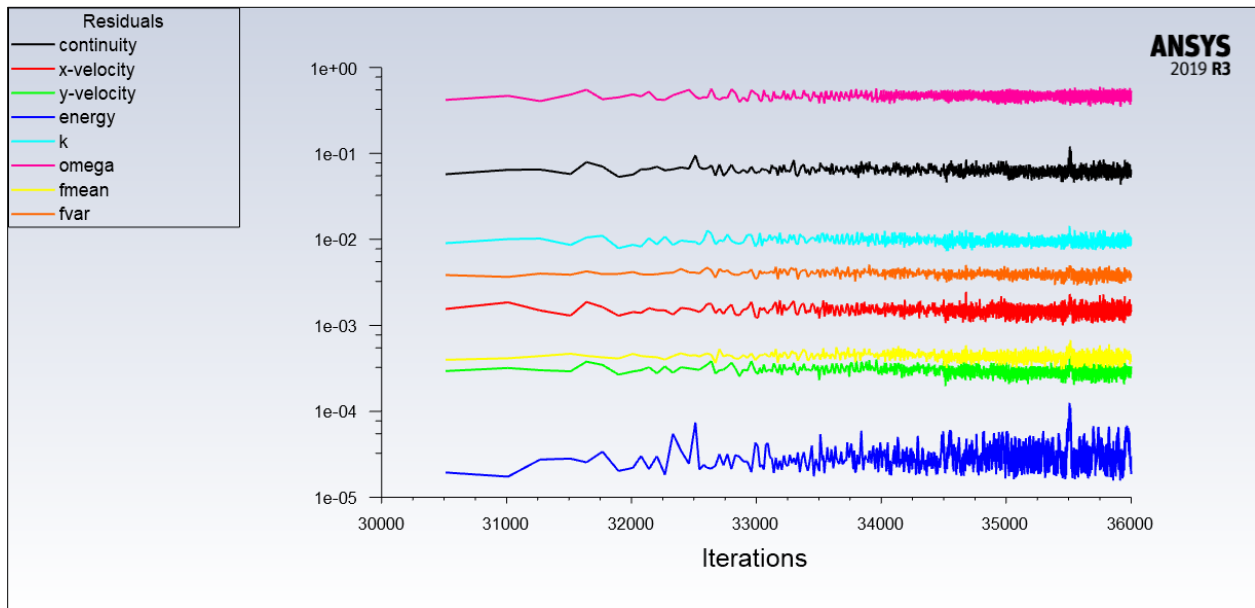


Figure 4.22: Residuals for the structured axisymmetric mesh

The report plots appear to show that convergence is being reached with Figure 4.20 showing the near-complete combustion of Hydrogen. While steady state residuals would show the residual trends decreasing for convergence, the residuals alone cannot be relied upon to determine convergence in a transient simulation. A mix of the solution report plots, residuals, and contours need to be evaluated to determine convergence. Thus far, the residuals are not showing any sudden divergences or changes in trend, the fact that they are stable are signs of convergence.

However, various warnings appeared on the output console for ANSYS Fluent with warnings such as “minimum PDF table enthalpy exceeded” or “turbulent viscosity limited to viscosity ratio.” These warnings appear to be due to the mesh itself not being adequately generated. Because of these issues, we opted for utilizing the unstructured mesh to try and prevent these errors from occurring.

4.2 Current Results

4.2.1 Unstructured Axisymmetric Mesh

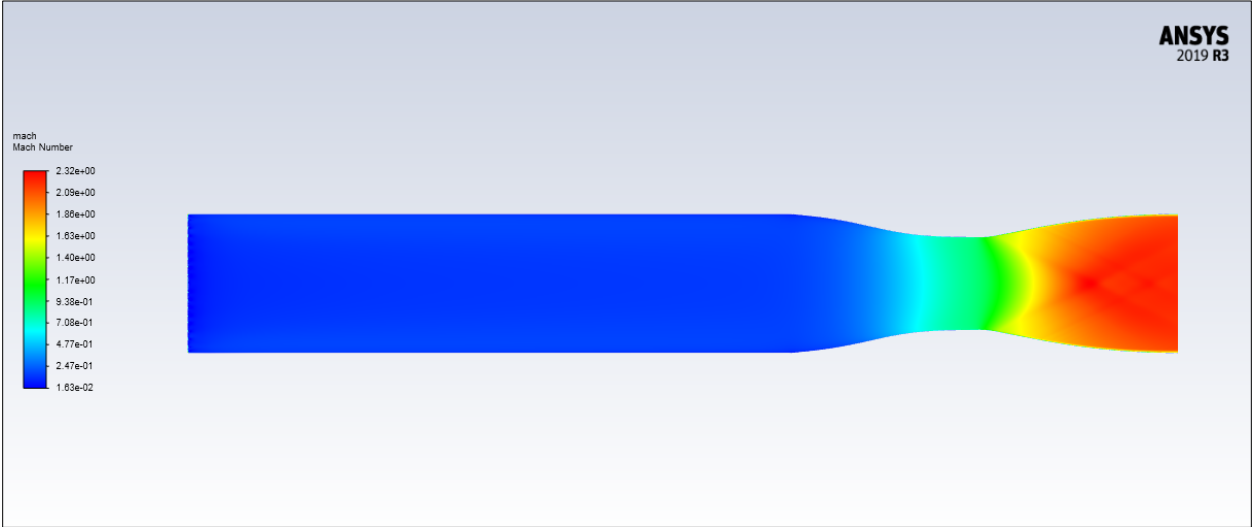


Figure 4.23: Mach contours for the unstructured mesh

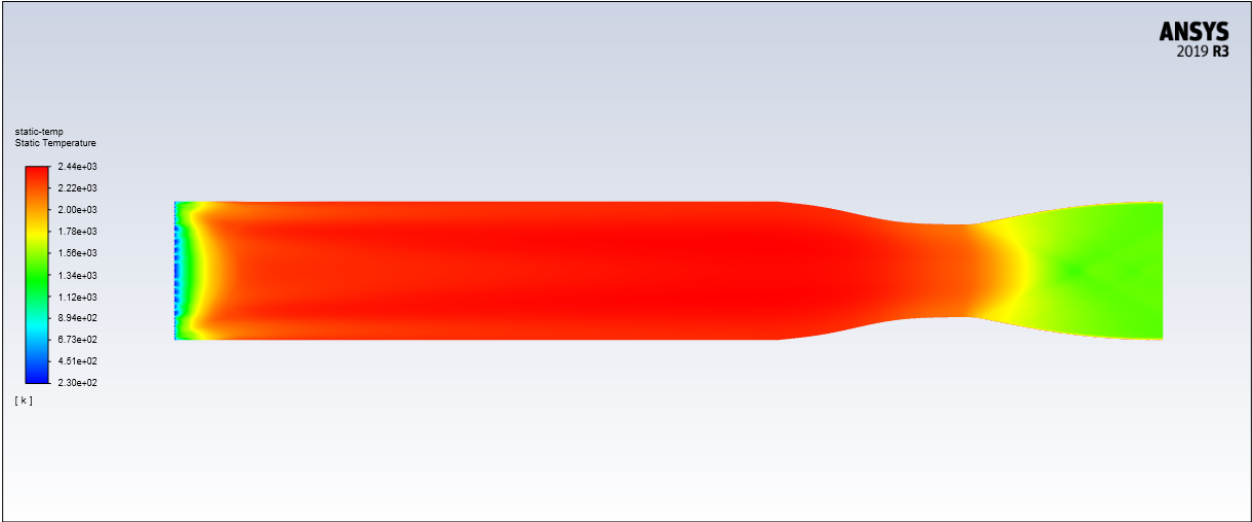


Figure 4.24: Static temperature contours for the unstructured mesh

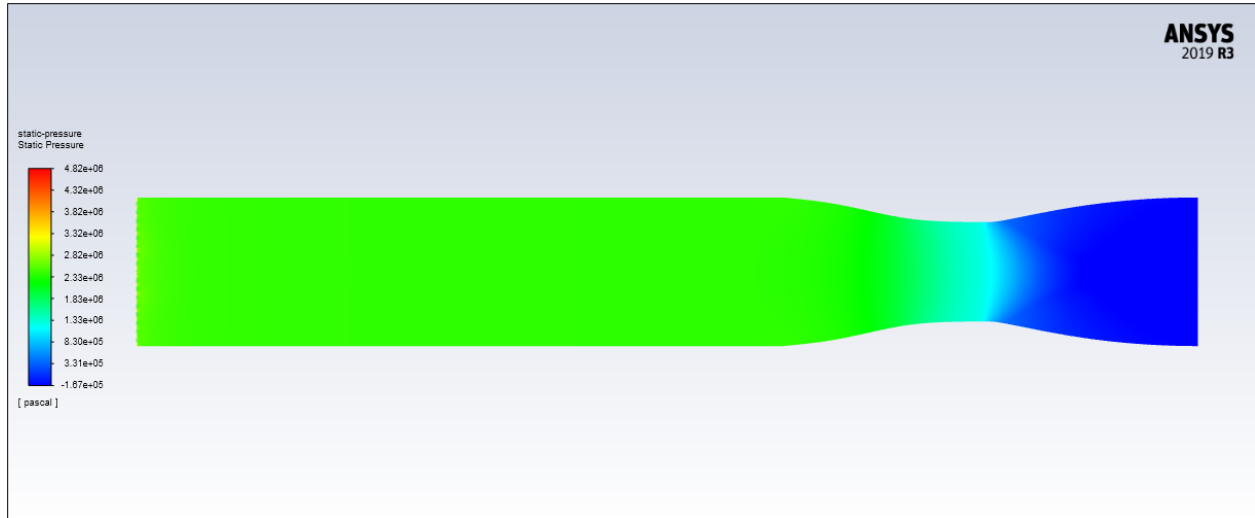


Figure 4.25: Static pressure contours for the unstructured mesh

For our first unstructured mesh simulation we opted for using a timestep of 0.0001 just as we did for the structured axisymmetric mesh. However, as seen in Table 4.4, our static pressure values are significantly improved compared to the structured axisymmetric mesh.

Table 4.4: Comparison of outlet conditions for the unstructured axisymmetric model

	Expected Outlet Conditions	Area Weighted Average in Simulated Outlet
M_{10}	1.806	2.149
P_{10} (kPa)	55.47	48.45
T_{10} (K)	1106.68	1515.6

Despite the improved static pressure values from the unstructured axisymmetric mesh, our Mach and static temperature values are still not matching our expected outlet conditions.

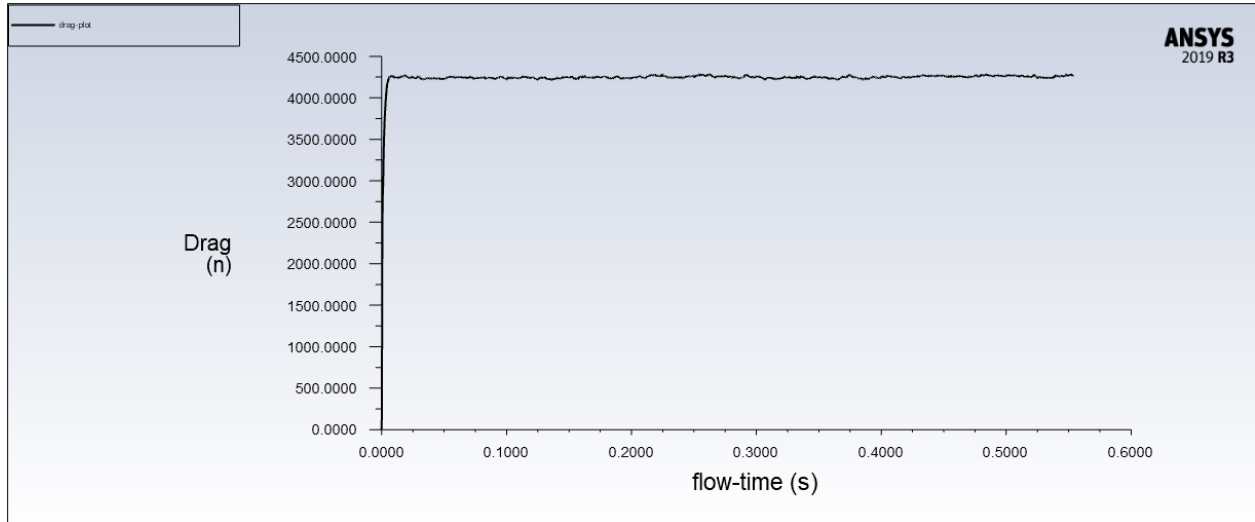


Figure 4.26: Drag force near walls for the unstructured axisymmetric mesh

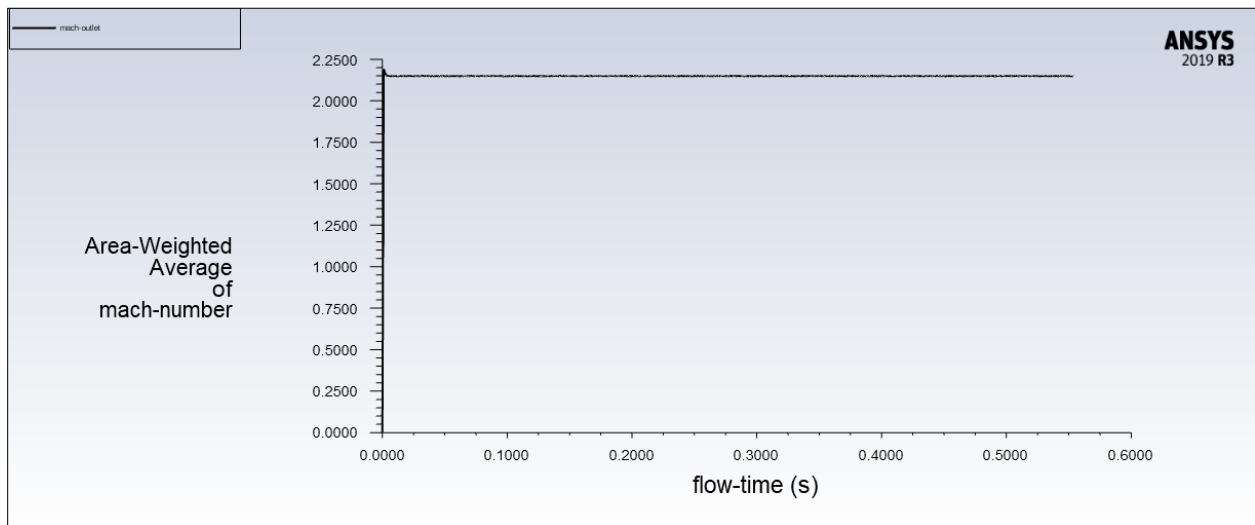


Figure 4.27: Area-weighted average of outlet Mach for the unstructured axisymmetric mesh

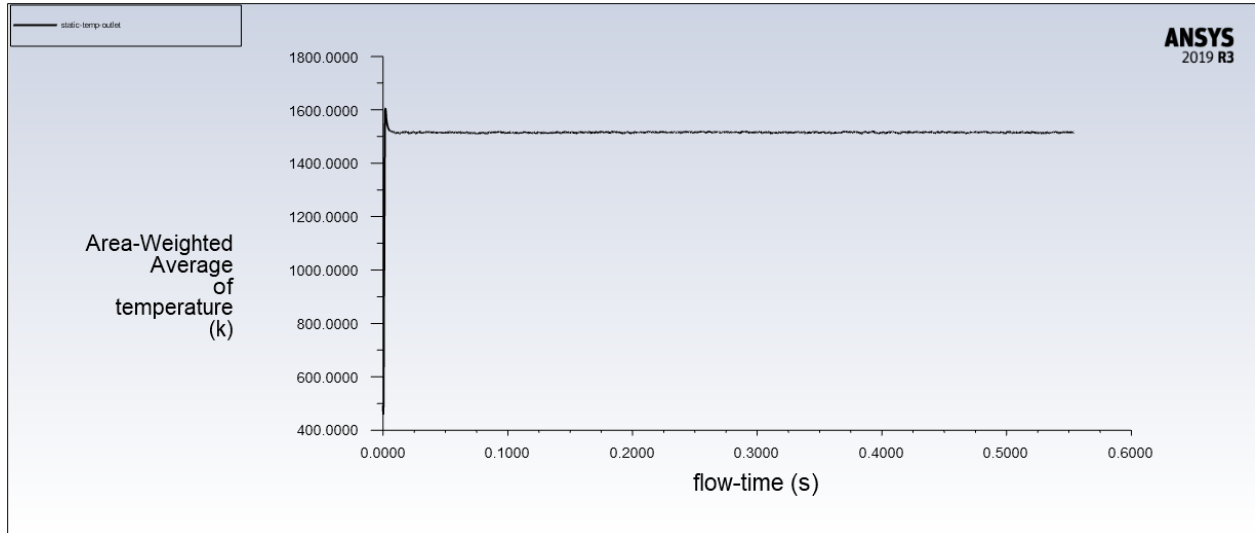


Figure 4.28: Area-weighted average of static temperature at the outlet for the unstructured axisymmetric mesh

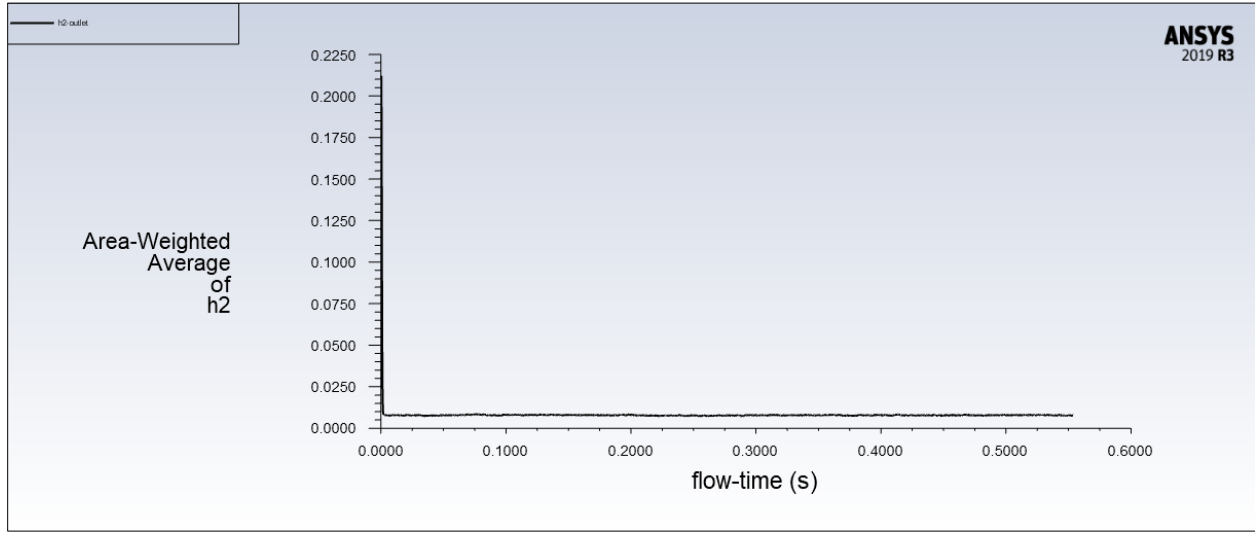


Figure 4.29: Area-weighted average of hydrogen at the outlet for the unstructured axisymmetric mesh

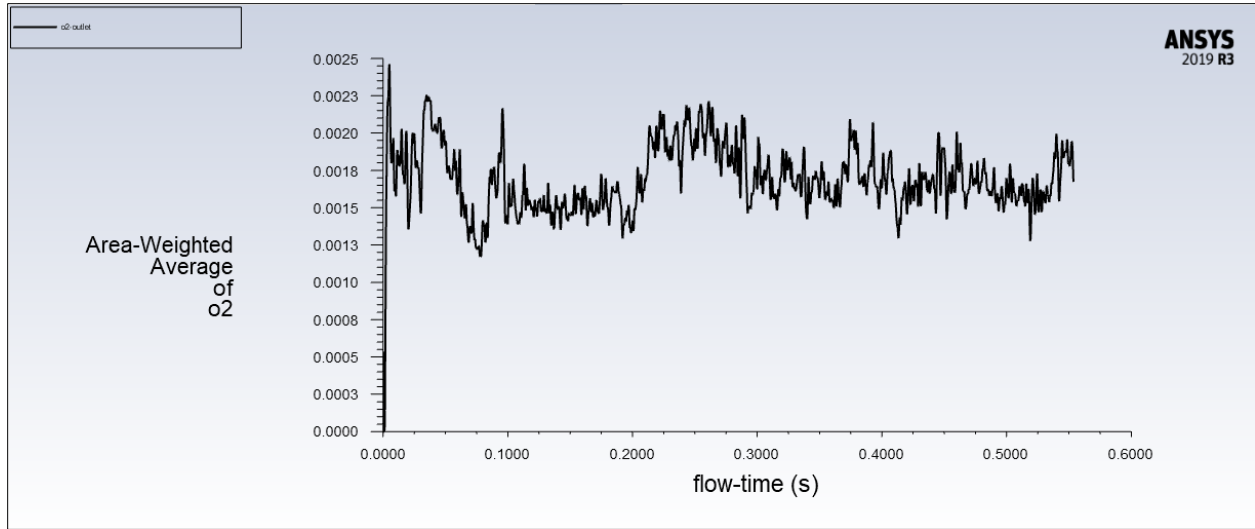


Figure 4.30: Area-weighted average of oxygen at the outlet for the unstructured axisymmetric mesh

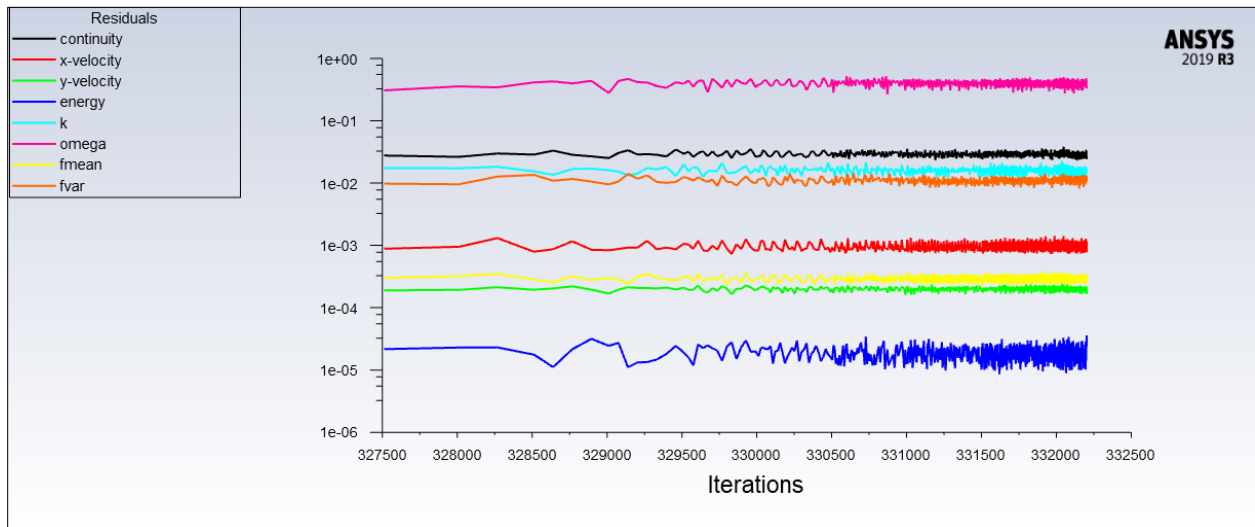


Figure 4.31: Residuals for the unstructured axisymmetric mesh

The report plots and the residuals plot show that convergence is being reached with Figure 4.29 showing the near-complete combustion of Hydrogen. The lack of sudden divergences or changes in overall trend for the residuals and the solution report plots shows that convergence is being reached.

4.2.2 Unstructured Axisymmetric Mesh with a smaller time step

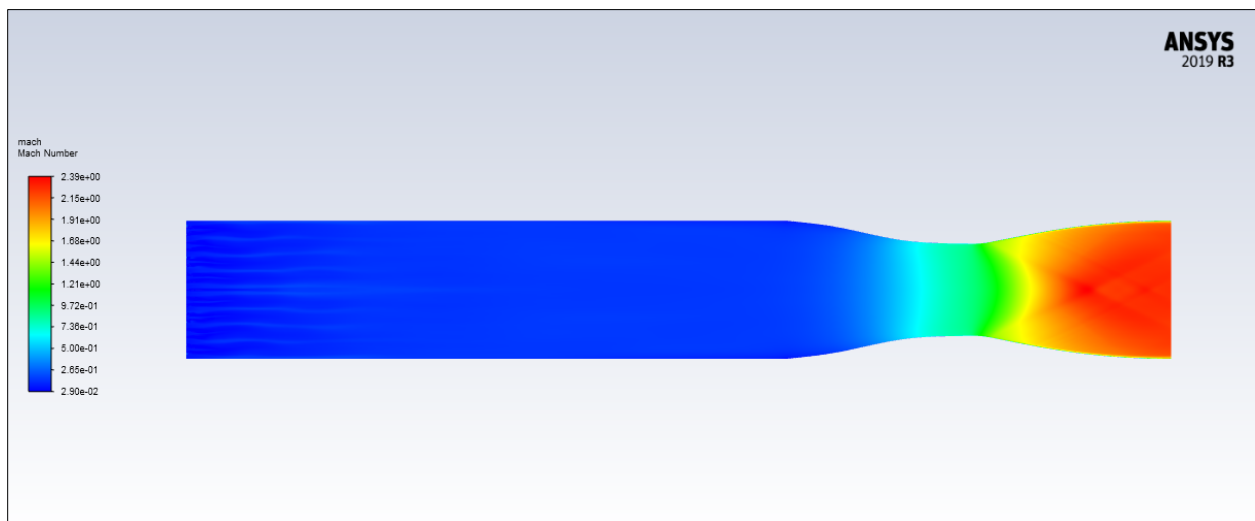


Figure 4.32: Mach contours for the unstructured mesh with a reduced time step

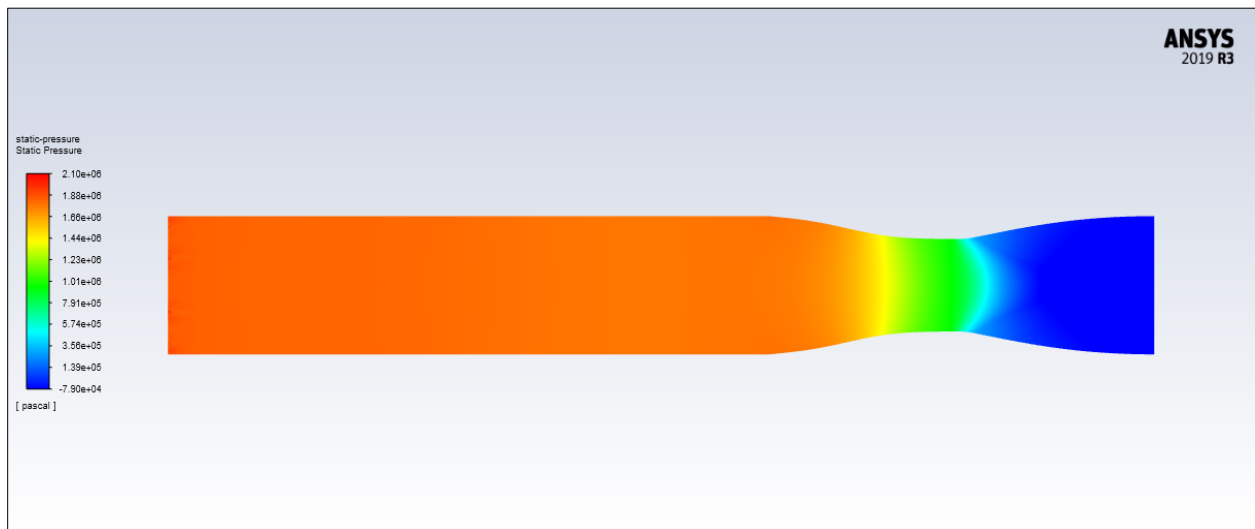


Figure 4.33: Static pressure contours for the unstructured mesh with a reduced time step

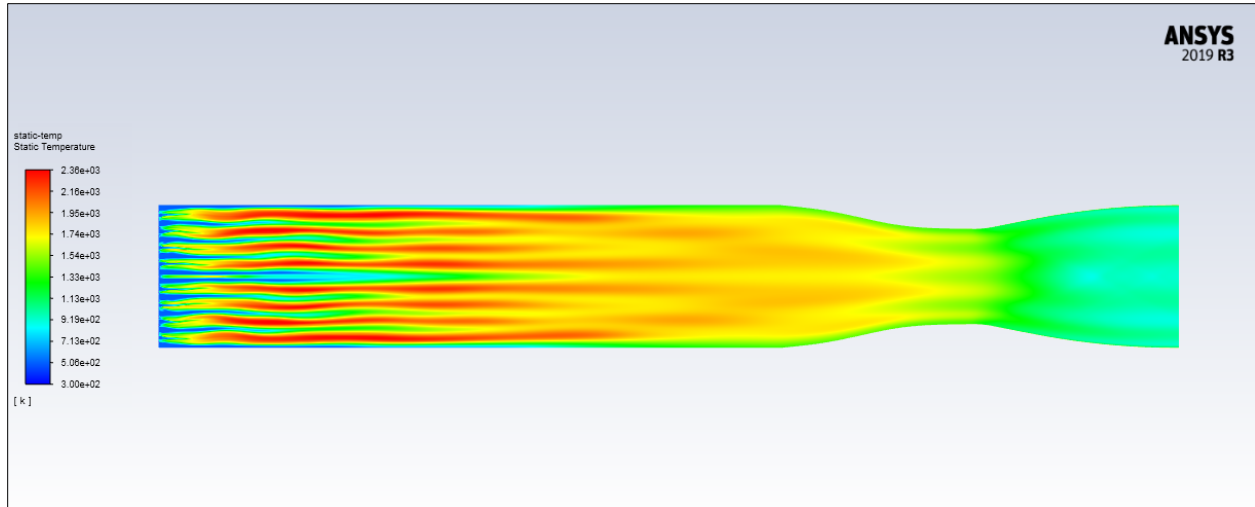


Figure 4.34: Static temperature contours for the unstructured mesh with a reduced time step

For the unstructured mesh we decided to reduce the time step size to 0.00001 to increase the accuracy of our simulation. While the Mach and static pressure contours stayed similar, the static temperature contours in Figure 4.34 showed that the Hydrogen fuel from the injectors was not immediately mixing until the latter half of the combustion chamber itself.

Table 4.5: Comparison of outlet conditions for the unstructured axisymmetric model

	Expected Outlet Conditions	Area Weighted Average in Simulated Outlet
M_{10}	1.806	2.183
P_{10} (kPa)	55.47	-30.17
T_{10} (K)	1106.68	1043.1

Table 4.5 shows that our simulated static pressure is a negative value just as it was in Table 4.3 when we expected the smaller time step to give a similar pressure value to Table 4.4 when the same unstructured mesh was simulated for a higher time step. However, our static temperature at the outlet is now closer to the expected outlet static temperature.

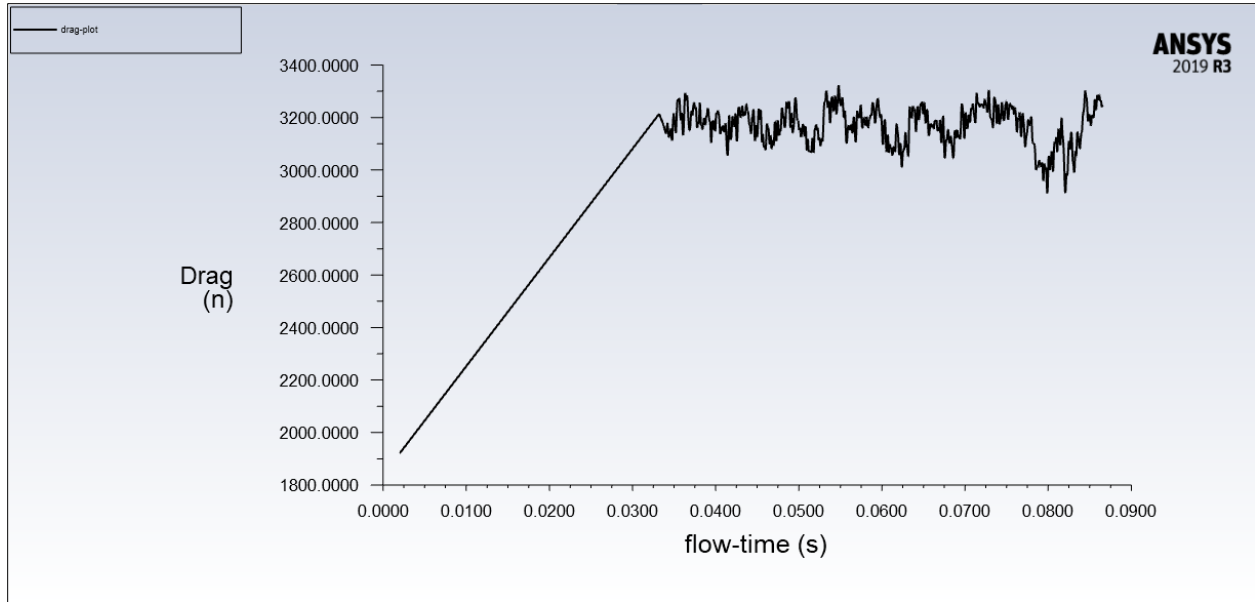


Figure 4.35: Drag force near walls for the unstructured mesh with a reduced time step

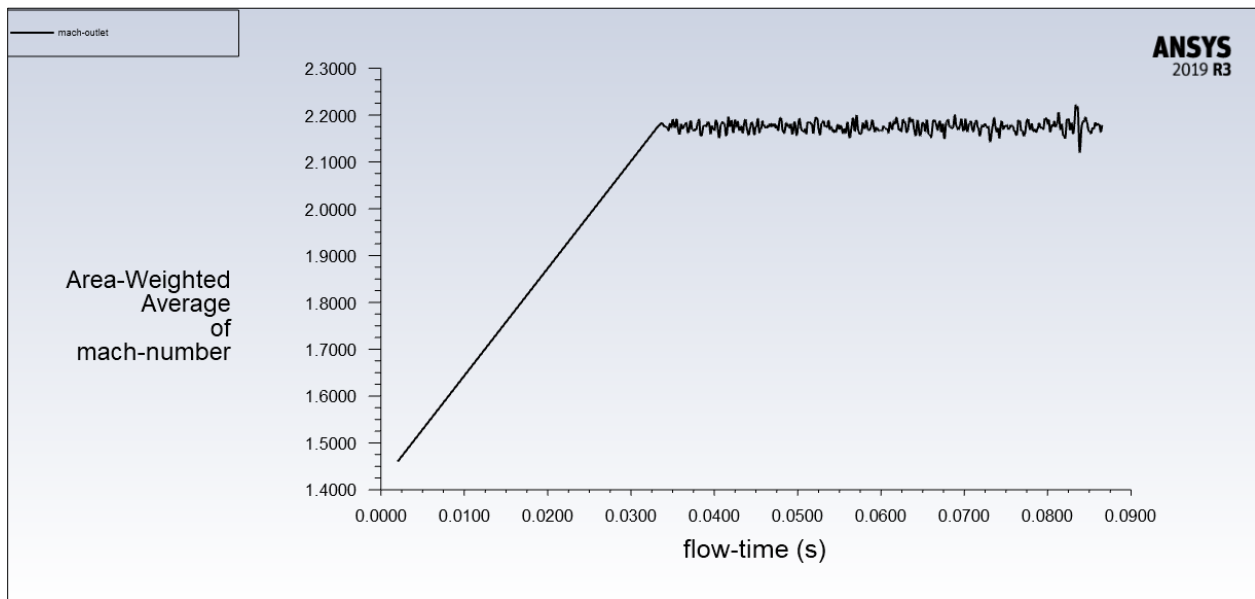


Figure 4.36: Area-weighted Mach number at the outlet for the unstructured mesh with a reduced time step

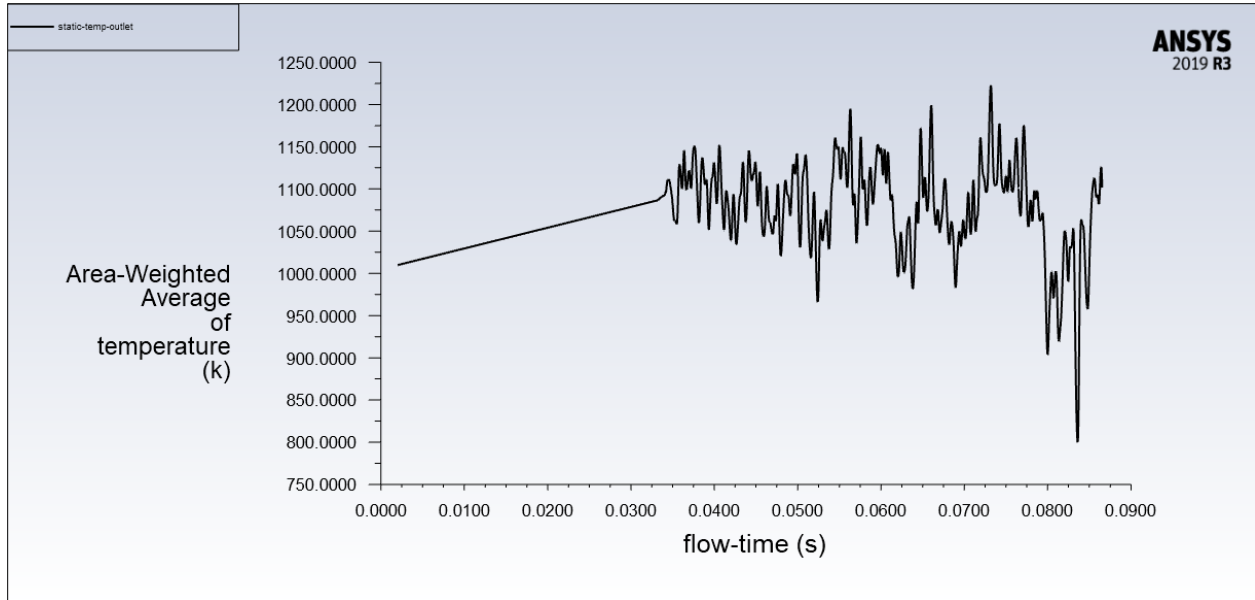


Figure 4.37: Area-weighted average of static temperature at the outlet for the unstructured mesh with a reduced time step

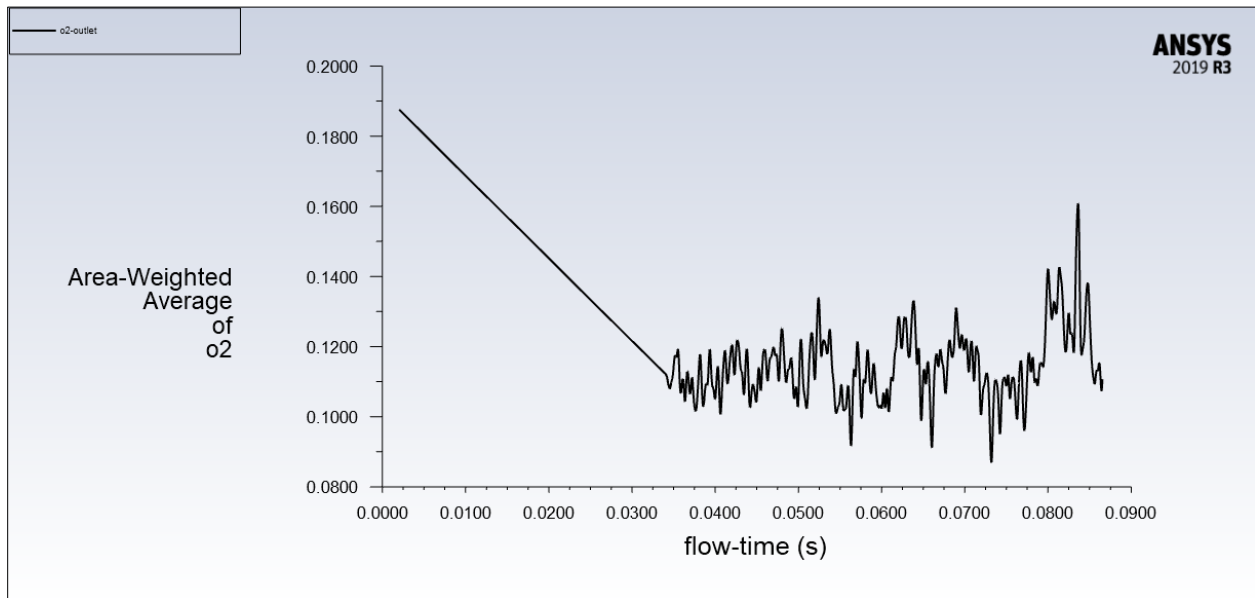


Figure 4.38: Area-weighted average of oxygen at the outlet for the unstructured mesh with a reduced time step

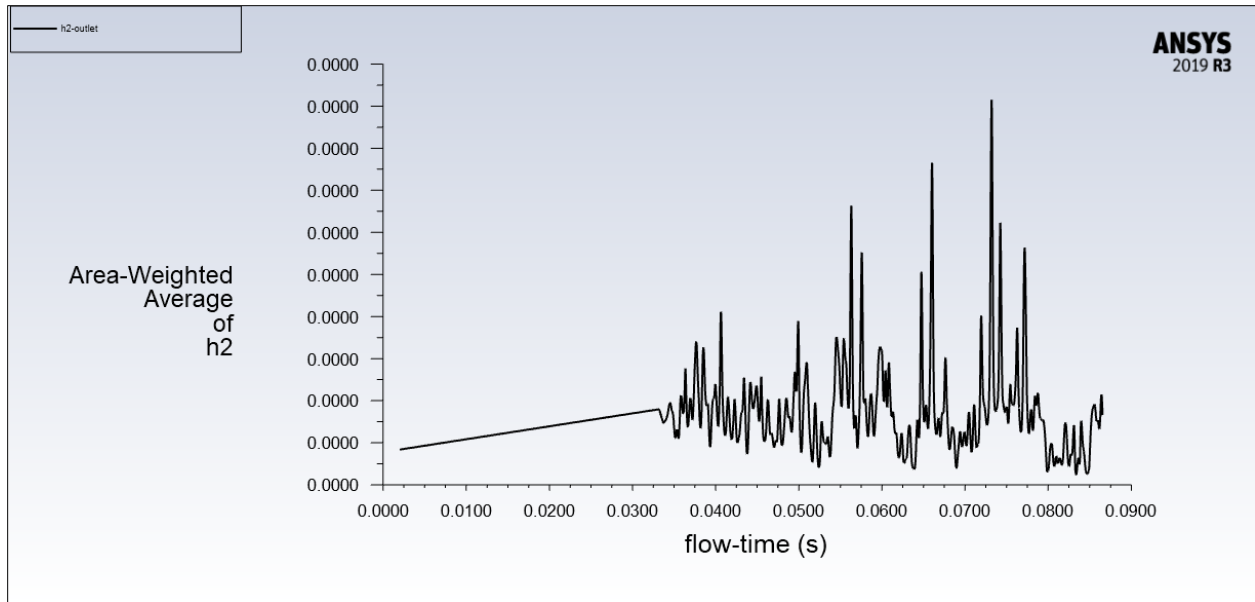


Figure 4.39: Area-weighted average of hydrogen at the outlet for the unstructured mesh with a reduced time step

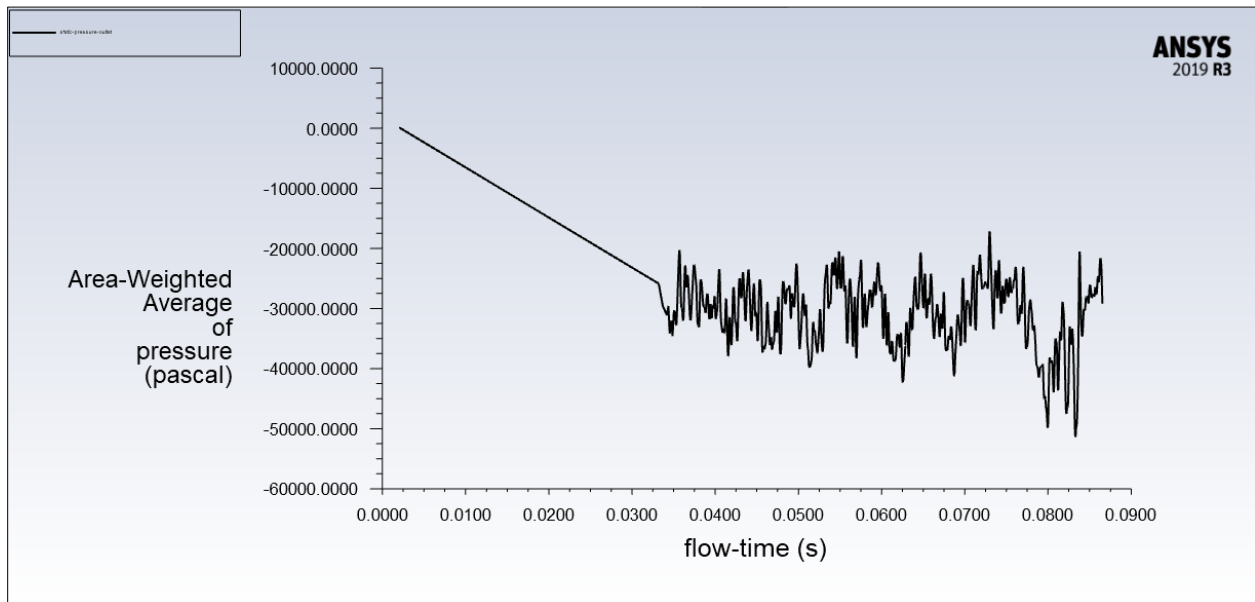


Figure 4.40: Area-weighted average of static pressure at the outlet for the unstructured mesh with a reduced time step

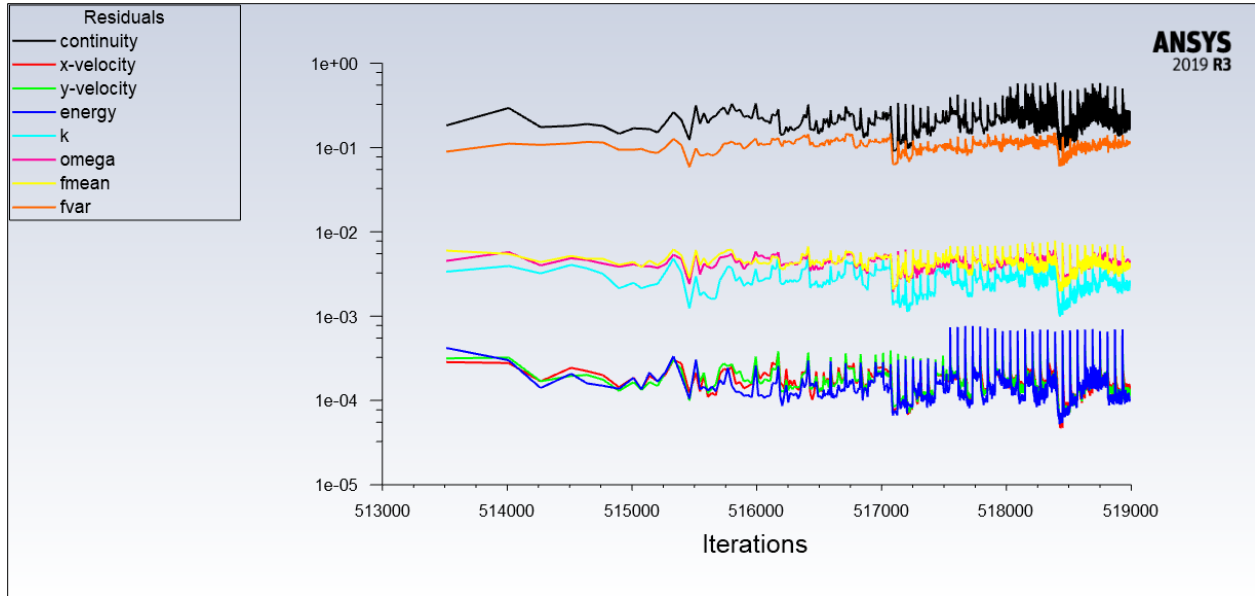


Figure 4.41: Residuals for the unstructured mesh with a reduced time step

For the simulation with the reduced time step, a solution plot (Figure 4.40) was generated to show the static pressure progression at the outlet as the simulation progressed. While the residuals in Figure 4.41 show that convergence is starting to take place, the solution plots for Figures 4.36 through 4.39 aren't showing signs of convergence due to the sudden spikes we see in the solution plots. This could explain why our static pressure value in Table 4.5 is negative and it could explain the nature of our static temperature contours in Figure 4.34.

While Figure 4.39 does show the near-complete combustion of Hydrogen as we saw in previous simulations, it does not appear to be converged either. We do however see that the solution plots for Drag Force near the walls (Figure 4.35) and the area-weighted Mach number at the outlet (Figure 4.36) are steady enough to be considered converged.

As noted earlier, the Mach values were significantly higher than the design Mach of our analytically derived nozzle while the density-based results showed Mach values that were just slightly lower than the nozzle design Mach. The reduced Mach value is to be expected due to viscosity losses from the boundary layer. However, the increase in Mach number for the pressure-based simulations are inaccurate. The dubious Mach values from the pressure-based studies are due to the shortcomings of the pressure-based solver when it is utilized in a compressible flow as mentioned before in Section 1.2.6.

5. Conclusions and Recommendations

This conceptual study has aided in providing a framework for future internal combustible flow studies and for verifying the possible limitations of our analytically derived model. It can also be concluded that the density-based solver is the most viable solver for our internal combustible flow scenario.

As such, for future efforts it is recommended that a density-based solver is utilized to fully account for compressible flow phenomena. Our most accurate area weighted average results came from our density-based studies despite the issues with combustion and flow mixing that were shown by the contours. However, this can likely be fixed by altering the fuel injector design and layout along with altering the boundary conditions to try and allow for improved fuel mixing. It is also recommended to utilize the transient model instead of the steady-state model to account for inherently transient propulsion processes such as ignition [21].

The pressure-based simulations only produced an accurate static temperature value when the time step was reduced. The pressure-based contours showed full mixture and fuel combustion despite the issues regarding area weighted average results. The pressure-based solver may allow for passable contours but should not be relied upon for computational analyses in compressible flow environments.

It was initially thought that the internal flow simulation could be executed with only the combustion chamber and the nozzle itself with the assumption that the analytically derived station 3 air and fuel conditions could be used as our boundary conditions. It is possible that our lack of an inlet section on our model may have led to our divergence issues with the density-based solver. This is because the inlet section is necessary to adequately account for compressibility effects that are inflicted by the ramjet's inlet and to accurately model the internal boundary layer which is coupled with the boundary layer that results from the inlet section. As such, another recommendation is to also simulate the ramjet inlet section for improved accuracy in future studies.

References

- [1] Ingenito, A., *Subsonic Combustion Ramjet Design*, Springer, Switzerland, 2021, Chap. 2.
- [2] Rogoway, T., "Is the European Meteor Air-To-Air Missile Really the Best in the World?" *The Drive*, 2 Aug. 2016, [Online], Available: <https://www.thedrive.com/the-war-zone/4678/is-the-european-meteor-air-to-air-missile-really-the-best-in-the-world>
- [3] Babu, V., "Run Like the Wind," *ANSYS Advantage*, Vol. VIII, No. 1, 2014, pp. 32-36.
- [4] Clark, R. J., "Numerical Simulation and Modeling of Combustion in Scramjets," Ph.D. Dissertation, Mechanical and Aerospace Engineering Dept., Western Michigan University, Kalamazoo, MI, 2015.
- [5] Gruber, M. R., Baurle, R. A., Mathur, T., and Hsu, K. Y., "Fundamental Studies of Cavity-Based Flameholder Concepts for Supersonic Combustors," *Journal of Propulsion and Power*, Vol. 17, No. 1, 2001, pp. 146-153. doi: 10.2514/2.5720
- [6] ANSYS, ANSYS Fluent Theory Guide, Ver. 14.5, ANSYS, Inc., Canonsburg, PA, 2011.
- [7] Cabell, K. F., Drozda, T. G., Axdahl, E. L., and Danehy, P. M., "The Enhanced Injection and Mixing Project at NASA Langley," *JANNAF CS/APS/EPSS/PSHS Joint Subcommittee Meeting*, 2014.
- [8] Drozda, T. G., Drummond, J. P., and Baurle, R. A., "CFD Analysis of Mixing Characteristics of Several Fuel Injectors at Hypervelocity Flow Conditions," *52nd AIAA/SAE/ASEE Joint Propulsion Conference*, AIAA 2016-4764, Salt Lake City, UT, 2016.
- [9] Dorfman, A., *Classical and Modern Engineering Methods in Fluid Flow and Heat Transfer: An Introduction for Engineers and Students*, Momentum Press, New York, 2013, Chaps. 3, 8, 9.
- [10] Kummitha, O. R., Pandey, K. M., and Gupta, R., "CFD analysis of a scramjet combustor with cavity based flame holders," *Acta Astronautica*, Vol. 144, Mar. 2018, pp. 244-253. <https://doi.org/10.1016/j.actaastro.2018.01.005>
- [11] Berglund, M., Fedina, E., Fureby, C., Tegnér, J., and Sabel'nikov, V., "Finite Rate Chemistry Large-Eddy Simulation of Self-Ignition in Supersonic Combustion Ramjet," *AIAA Journal*, Vol. 48, No. 3, 2010, pp. 540-550. doi: 10.2514/1.43746

- [12] Sudarma, A. F., and Morsy, M. H., “Numerical study of non-premixed air-methane swirl combustor flows using RANS method,” *IOP Conference Series: Materials Science and Engineering*, Vol. 453, Jakarta, Indonesia, 2018.
- [13] Lewandowski, M. T., and Pozorski, J., “Assessment of turbulence-chemistry interaction models in the computation of turbulent non-premixed flames,” *Journal of Physics: Conference Series*, Vol. 760, Słok, Bełchatów, Poland, 2016.
- [14] Nelson, D., “CFD Analysis of Fuel Injector Performance Within a Dual Mode Ramjet Combustor,” Thesis, Dept. of Mechanical and Aerospace Engineering., California State University, Long Beach, Long Beach, CA, 2020.
- [15] Vergine, F., “Simulations From 01/22/2021,” Department of Aerospace Engineering., San Jose State University, San Jose, CA, 2021.
- [16] Boyer, K., Mattingly, J. D., *Elements of Propulsion: Gas Turbines and Rockets*, 2nd ed., American Institute of Aeronautics and Astronautics, Inc., Reston, VA, 2016, Chap. 11
- [17] Anderson, J., *Fundamentals of Aerodynamics*, 6th ed., McGraw Hill, New York, 2017, Chaps. 7, 8, 9, 10.
- [18] Oevermann, M., “Numerical investigation of turbulent hydrogen combustion in a SCRAMJET using flamelet modeling”, *Aerospace Science and Technology*, Vol 4, Issue 7, 2000, pp. 463-480. [https://doi.org/10.1016/S1270-9638\(00\)01070-1](https://doi.org/10.1016/S1270-9638(00)01070-1)
- [19] Smith, G., P. et al, “GRI-Mech 3.0,” CHEMKIN Database, retrieved 12 October 2021 <http://combustion.berkeley.edu/gri-mech/version30/text30.html>
- [20] ANSYS, ANSYS Fluent Theory Guide, Ver. 12.0/12.1, ANSYS, Inc., Canonsburg, PA, 2009.
- [21] Zubanov, V. M., Stepanov, D. M., Shabliy, L. S., “The technique for Simulation of Transient Combustion Processes in the Rocket Engine Operating with Gaseous Fuel ‘Hydrogen and Oxygen,’” *Journal of Physics: Conference Series*, Vol. 803, Tomsk, Russia, 2016.

Appendix: Coordinate Points for Mach 1.806 Nozzle

Polyline=true			1	0.009238901	0.024251291
1	0.100393029	0.034942416	1	0.008785733	0.02416207
1	0.096323094	0.034921853	1	0.008322302	0.024075635
1	0.092321019	0.03486119	1	0.007858022	0.023993887
1	0.08839376	0.034761961	1	0.007392938	0.023916834
1	0.084535966	0.03462547	1	0.006927101	0.023844485
1	0.08074195	0.034452835	1	0.006460556	0.023776847
1	0.077005542	0.034244971	1	0.005993351	0.023713926
1	0.073319949	0.034002554	1	0.005525535	0.023655729
1	0.069677519	0.033725986	1	0.005057154	0.023602262
1	0.066069376	0.033415324	1	0.004588258	0.02355353
1	0.062484983	0.033070186	1	0.004118892	0.023509539
1	0.058911364	0.032689604	1	0.003649106	0.023470292
1	0.05533195	0.032271787	1	0.003178948	0.023435795
1	0.05172466	0.031813723	1	0.002708465	0.02340605
1	0.048058395	0.031310478	1	0.002237706	0.02338106
1	0.044286428	0.030753836	1	0.001766716	0.023360829
1	0.040332073	0.03012939	1	0.001295548	0.023345357
1	0.036052646	0.029409217	1	0.000824248	0.023334647
1	0.031121777	0.028528092	1	0	0.023327366
1	0.022497979	0.026863163			